nature biomedical engineering

ARTICLES

https://doi.org/10.1038/s41551-022-00912-3

Check for updates

Revealing nanostructures in brain tissue via protein decrowding by iterative expansion microscopy

Deblina Sarkar[1,2,17], Jinyoung Kang[3,17], Asmamaw T. Wassie[4,17], Margaret E. Schroeder[3,5], Zhuyu Peng[5,6], Tyler B. Tarr[7], Ai-Hui Tang[7,8], Emily D. Niederst[6], Jennie Z. Young[5,6], Hanquan Su[9,10], Demian Park[3], Peng Yin[9,10], Li-Huei Tsai[5,6,11] ✉, Thomas A. Blanpied[7,12] ✉ and Edward S. Boyden[2,3,4,5,13,14,15,16] ✉

Many crowded biomolecular structures in cells and tissues are inaccessible to labelling antibodies. To understand how proteins within these structures are arranged with nanoscale precision therefore requires that these structures be decrowded before labelling. Here we show that an iterative variant of expansion microscopy (the permeation of cells and tissues by a swellable hydrogel followed by isotropic hydrogel expansion, to allow for enhanced imaging resolution with ordinary microscopes) enables the imaging of nanostructures in expanded yet otherwise intact tissues at a resolution of about 20 nm. The method, which we named 'expansion revealing' and validated with DNA-probe-based super-resolution microscopy, involves gel-anchoring reagents and the embedding, expansion and re-embedding of the sample in homogeneous swellable hydrogels. Expansion revealing enabled us to use confocal microscopy to image the alignment of pre-synaptic calcium channels with post-synaptic scaffolding proteins in intact brain circuits, and to uncover periodic amyloid nanoclusters containing ion-channel proteins in brain tissue from a mouse model of Alzheimer's disease. Expansion revealing will enable the further discovery of previously unseen nanostructures within cells and tissues.

There is great desire to understand how proteins are arranged, with nanoscale precision, within cells and tissues. Super-resolution microscopy has offered the capability of combining biomolecular recognition with nanoscale optical resolution through staining with target protein-specific antibodies[1]. However, such techniques are limited by the accessibility of labels to the biomolecules to be imaged, because it is the labels that are visualized, not the biomolecules themselves. Many crowded, biomolecule-rich structures are at the core of biological functions and disease states, with inter-protein distances being smaller than the size of antibodies, which may thus prohibit access to biomolecules of interest by labels. Overcoming this issue requires a technology that can not only achieve super-resolution down to the low tens of nanometres, but also enable decrowding of biomolecules in cells and tissues.

We reasoned that to decrowd proteins from each other, we could leverage the spatial expansion property of expansion microscopy (ExM)[2,3] in which cells and tissues are densely permeated by an even mesh of swellable hydrogel, and then expanded to obtain enhanced resolution on ordinary microscopes. To establish decrowding and simultaneously achieve resolution on par with the best classical super-resolution techniques (down to ~20 nm resolution), we combined the expansion principle with a scheme for biomolecular preservation to build a technology that we term expansion revealing (ExR). By direct comparison of biomolecular structures where labelling was done in the normal crowded environment vs after the decrowding effect of ExR, with both being imaged at the same level of resolution, we demonstrate that ExR indeed reveals previously unknown biological information and can indeed lead to the discovery of nanostructures in brain tissue that would otherwise have remained invisible. We anticipate that ExR will enable the visualization of a variety of previously undescribed biological nanostructures. We illustrate the capabilities of ExR by unmasking key components of synaptic nanocolumns as well as periodic nanostructures potentially of relevance to Alzheimer's disease, both in mouse brain tissue.

Results

ExR enables simultaneous super-resolution and decrowding. To achieve super-resolution down to the low tens of nanometres, two rounds of expansion (or 15–20X expansion factor) are required. One would ideally minimally alter the proteins during the expansion process while decrowding them from one another as much as

[1]Media Lab, MIT, Cambridge, MA, USA. [2]MIT Center for Neurobiological Engineering, MIT, Cambridge, MA, USA. [3]MIT McGovern Institute for Brain Research, MIT, Cambridge, MA, USA. [4]Department of Biological Engineering, MIT, Cambridge, MA, USA. [5]Department of Brain and Cognitive Sciences, MIT, Cambridge, MA, USA. [6]The Picower Institute for Learning and Memory, MIT, Cambridge, MA, USA. [7]Department of Physiology, University of Maryland School of Medicine, Baltimore, MD, USA. [8]CAS Key Laboratory of Brain Function and Disease, Biomedical Sciences and Health Laboratory of Anhui Province, Division of Life Sciences and Medicine, University of Science and Technology of China, Hefei, China. [9]Wyss Institute for Biologically Inspired Engineering, Harvard University, Boston, MA, USA. [10]Department of Systems Biology, Harvard Medical School, Boston, MA, USA. [11]Broad Institute of MIT and Harvard, Cambridge, MA, USA. [12]Program in Neuroscience, University of Maryland School of Medicine, Baltimore, MD, USA. [13]Koch Institute, MIT, Cambridge, MA, USA. [14]Howard Hughes Medical Institute, Cambridge, MA, USA. [15]Media Arts and Sciences, MIT, Cambridge, MA, USA. [16]K. Lisa Yang Center for Bionics, MIT, Cambridge, MA, USA. [17]These authors contributed equally: Deblina Sarkar, Jinyoung Kang, Asmamaw T Wassie. ✉e-mail: lhtsai@mit.edu; TBlanpied@som.umaryland.edu; edboyden@mit.edu

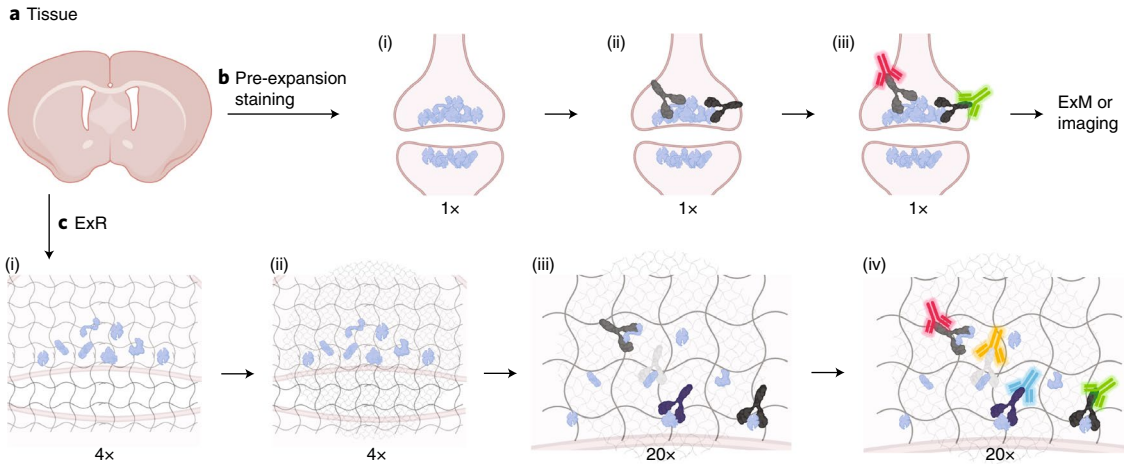

Fig. 1 | ExR, a technology for decrowding of proteins through isotropic protein separation. a, Schematic of coronal section of mouse brain before staining or expansion. **b**, Conventional antibody staining may not detect crowded biomolecules, shown here in pre- and post-synaptic terminals of cortical neurons. (**i**) Crowded biomolecules before antibody staining. (**ii**) Primary antibody (Y-shaped proteins) staining in non-expanded tissue. Antibodies cannot access interior biomolecules, or masked epitopes of exterior biomolecules. (**iii**) Secondary antibody (fluorescent green and red Y-shaped proteins) staining in non-expanded tissue. After staining, tissue can be imaged or expanded using earlier ExM protocols, but inaccessible biomolecules will not be detected. **c**, Post-expansion antibody staining with ExR. (**i**) Anchoring and first gelation step. Specimens are labelled with gel-anchoring reagents to retain endogenous proteins, with acrylamide included during fixation to serve as a polymer-incorporatable anchor, as in refs. [56,58]. Subsequently, the specimen is embedded in a swellable hydrogel that permeates densely throughout the sample (grey wavy lines), mechanically homogenized via detergent treatment and heat treatment, and expanded in water. (**ii**) Re-embedding and second swellable gel formation gelation. The fully expanded first gel (expanded 4X in linear extent) is re-embedded in a charge-neutral gel (not shown), followed by the formation of a second swellable hydrogel (light grey wavy lines). (**iii**) 20X expansion and primary antibody staining. The specimen is expanded by another factor of 4X via the addition of water, for a total expansion factor of ~20X, then incubated with conventional primary antibodies. Because expansion has decrowded the biomolecules, conventional antibodies can now access interior biomolecules and additional epitopes of exterior molecules. (**iv**) Post-expansion staining with conventional fluorescent secondary antibodies (fluorescent blue and yellow Y-shaped proteins, in addition to the aforementioned red and green ones) to visualize decrowded biomolecules. Schematic created with BioRender.com.

possible. To satisfy these conflicting requirements, ExR (Fig. 1a–c) achieves this with a new scheme. We reasoned that one could expand a brain specimen through one round of gelation and expansion, and that this first swellable hydrogel could then be further expanded if we formed a second swellable hydrogel in the space opened up by the first expansion, and then iteratively swelled the specimen a second time (see Methods for details). The proteins, being anchored to the first hydrogel throughout the entire process, would be retained because the original hydrogel would be further expanded by the second swellable hydrogel, and not cleaved or discarded. Thus, ExR imposes no extra processing steps on the proteins than is required for the first expansion. In the final step, the proteins can be antibody labelled (Fig. 1c) after decrowding and before imaging, enabling visualization of proteins that would have been missed if stained in the crowded state (Fig. 1b).

We first quantified the global isotropy of the expansion process in ExR and found a similar low distortion (that is, of a few percent over length scales of tens of microns, Supplementary Fig. 1) as we did for previous ExM protocols[3–7]. To measure effective resolution, we focused on synapses, given both their importance for neural communication and utility as a super-resolution testbed, staining post-expansion cortical synapses (Fig. 2a) with antibodies against the pre-synaptic protein Bassoon and the post-synaptic proteins PSD95 and Homer1, among other synaptic proteins (Fig. 2b–d). We found that when we measured the mean distance between domains containing the proteins PSD95, Homer1 and Shank3, we obtained values (Fig. 2e) that matched classical results found using stochastic optical reconstruction microscopy (STORM)[8] (note that our study focused on Shank3 and this earlier study focused on Shank1) in the low tens of nanometres. Thus, ExR exhibits effective resolution on the order of ~20 nm comparable to our earlier iterative expansion microscopy (iExM) protocol, which did not retain proteins[4].

To further validate the nanoscale precision of ExR, we compared pre-expansion DNA points accumulation for imaging in nanoscale topography (DNA-PAINT, a classical super-resolution method) and ExR, using the same specimen and the same field of view for comparison across the two technologies. We examined synaptic nanostructures stained with antibodies against synapsin using cultured neurons, which are amenable to classical high-precision super-resolution methods such as DNA-PAINT (see Methods). Both ExR and DNA-PAINT images show qualitatively similar staining patterns and resolution (Fig. 2f and Extended Data Fig. 1a–c). To quantitatively assess the nanoscale precision of ExR, we calculated, as a linearized distortion measure between ExR and PAINT, the shifts (in nm) between the half-maxima of the autocorrelation (ExR-ExR or PAINT-PAINT) and cross-correlation (ExR-PAINT) functions for single synaptic puncta imaged using both modalities (Extended Data Fig. 1d–f). Our analysis of 5 regions of interest (ROIs) from 3 wells of cultured neurons (1 culture batch) showed mean linearized distortion of 4.91 nm for the ExR-PAINT cross-correlation vs PAINT-PAINT autocorrelation (Fig. 2h, 95% CI of the mean (−29.93, 39.75)) and 18.78 nm for the ExR-PAINT cross-correlation vs ExR-ExR autocorrelation (Fig. 2i, 95% CI of the mean (−20.10, 57.66)). This analysis is a conservative one: ExR could in principle, through the decrowding effect (Fig. 1a–c), additionally alter the synapsin staining vs that of PAINT, but note that here, even if we conservatively lump all such decrowding-related changes into the category of distortion (as the above analysis does), we get an upper bound on the distortion in the low double-digit nanometres.

To compare the ability to distinguish between neighbouring nanostructures using DNA-PAINT and ExR, we examined pairs of neighbouring synaptic puncta (Extended Data Fig. 1g). We found that the absolute value of the difference in synaptic puncta distances as measured using ExR vs DNA-PAINT, normalized to the distance measured using DNA-PAINT, was ~11% (Fig. 2j, 95% CI of normalized absolute difference (0.06228, 0.1548); Extended Data Fig. 1i, 95% CI of difference between synaptic puncta centroid distance, PAINT-ExR: (−0.05419, 0.03649); see Supplementary Table 1 for detailed statistics; $n = 27$ pairs from 5 ROIs from 3 wells of cultured neurons from 1 culture batch). The coefficient of variation for distance between synaptic puncta imaged using ExR, calculated as the standard deviation of the difference in distance between pairs of synaptic puncta (PAINT-ExR) divided by the mean distance of the same pairs from DNA-PAINT, was 0.1367 ($n = 27$ cropped synaptic puncta pairs, 5 ROIs from 3 wells of neurons from 1 culture batch). Furthermore, we found no significant difference in the number of unique puncta detected after thresholding (Extended Data Fig. 1h, 95% CI of difference between number of synaptic puncta, PAINT-ExR: (−0.2936, 0.1336), $n = 50$ pairs, 5 ROIs from 3 wells of neurons from 1 culture batch). Similarly, we found no significant difference in the total number of synaptic puncta detected after thresholding across the entire imaging field of view (Extended Data Fig. 1j, paired t-test between ExR and DNA-PAINT images, $P = 0.9271$, $t = 0.09735$, d.f. = 4, $n = 5$ fields of view from 3 wells of neurons from 1 culture batch). Finally, analysis of the root mean square error (see Methods) between ExR and DNA-PAINT revealed low-percent error over a typical ROI size, comparable to previous expansion microscopy methods (that is, <50 nm error for measurement scales of ~4 μm and <150 nm error for measurement scales of ~15 μm; Fig. 2g). Thus, ExR exhibits a high degree of precision and low distortion compared with a classical high-resolution super-resolution method, DNA-PAINT.

High-fidelity enhancement of synaptic protein visualization via ExR. To gauge whether ExR could reveal nanostructures in the brain that were not visible without decrowding, and to further probe whether it incurred any costs in terms of decreased resolution or added distortion relative to classical staining (that is, pre-expansion staining and thus no decrowding), we devised a strategy where we would stain brain slices pre-expansion with an antibody against a synaptic protein, in such a way that antibodies would be anchored to the expansion hydrogel for later visualization. We then perform ExR and re-stain the same proteins with the same antibody a second time, thus enabling a within-sample comparison of a given protein across both conditions (with and without decrowding) at the same level of resolution to reveal any nanostructural differences. For pre-expansion staining (see Methods for details), we immunostained mouse brain slices containing somatosensory cortex (Fig. 3a) with primary antibodies followed by 6-((acryloyl)amino) hexanoic acid, succinimidyl ester (abbreviated AcX)-conjugated secondary antibodies, so that these antibodies could be attached to the swellable hydrogel for post-expansion tertiary antibody staining and visualization. This allowed us to compare pre-ExR staining to post-ExR staining at the same resolution level and for the same field of view, which are important for noticing any changes in nanostructural detail. We noted that Homer1 and Shank3 exhibited very similar visual appearances when we compared pre- vs post-ExR staining (quantified below), so we designated these two stains as 'reference channels', that is, co-stains that could help define synapses for the purposes of technological comparison, and that we could use to help us gauge whether other proteins were becoming more visible at synapses.

We chose 7 synaptic proteins important for neural architecture and transmission for this experiment—the pre-synaptic proteins Bassoon, RIM1/2 and the P/Q-type calcium channel $Ca_v2.1$ alpha 1A subunit, and the post-synaptic proteins Homer1, Shank3, SynGAP and PSD95 (Fig. 3b–h), staining for each protein along with a reference channel stain (note: when we imaged Homer1, we used Shank3 as the reference channel, and vice versa). These proteins were chosen on the basis of their frequent use as synaptic markers, their known interaction with one another and/or their functional importance at the synapse[9–15]. Specifically, Shank3 is a key post-synaptic scaffolding protein that interacts with PSD95 and Homer1, among other proteins, in the post-synaptic density[9], and Shank3 mutant mice display autistic-like behaviours and striatal changes[16]; RIM1/2 promotes calcium channel localization at the pre-synaptic active zone[17], controls synaptic vesicle release[18] and enhances the size of the readily releasable pool[17]; Bassoon and calcium channels contribute to vesicle release and promote vesicle reloading[19]; PSD95, another key post-synaptic scaffolding protein, drives maturation of excitatory synapses[20] and PSD95 mutant mice display enhanced long-term potentiation and impaired learning[21]; SynGAP regulates spine formation[14]; Homer and Shank form a higher-order complex that forms a binding platform for post-synaptic proteins[22].

Fig. 2 | Validation of ExR using synapses and comparison with DNA-PAINT. a, Low-magnification widefield image of a mouse brain slice stained with DAPI, with dotted box highlighting the somatosensory cortex used in subsequent figures for synapse staining. Scale bar, 500 μm. **b**–**d**, Confocal images (maximum intensity projections) of representative fields of view (cortical L2/3) and specific synapses after ExR expansion and subsequent immunostaining using antibodies against PSD95, Homer1 and Bassoon (**b**); Bassoon, Homer1 and Shank3 (**c**); and PSD95, RIM1/2 and Shank3 (**d**). Scale bar, 1 μm, left image; 100 nm, right images; in biological units (that is, the physical size divided by the expansion factor, used throughout the paper unless otherwise indicated). Shown are images from one representative experiment from two independent replicates. **e**, Measured distance between centroids of protein densities of PSD95 and Homer1, PSD95 and Shank3, and Shank3 and Homer1, in synapses such as those in **b**–**d**. The mean distance (again, in biological units) between PSD95 and Homer1 is 28.6 nm ($n = 126$ synapses from 3 slices from 1 mouse), 24.1 nm between PSD95 and Shank3 ($n = 172$ synapses from 3 slices from 1 mouse), and 17.6 nm between Shank3 and Homer1 ($n = 70$ synapses from 3 slices from 1 mouse). Mean ± s.e.m. are plotted; individual grey dots represent the measured distance for individual synapses. **f**, A pre-expansion DNA-PAINT image (left) and a registered confocal ExR image (maximum intensity projection, right) of the same field of cultured neurons after immunostaining with antibodies against Synapsin 1. Scale bar, 4 μm. Shown are images from one representative experiment from two independent replicates. **h**, Estimated population distribution (violin plot of density, with a dashed line at the median and dotted lines at the quartiles) of the shift (in nm) at which the correlation is half-maximal for PAINT-PAINT autocorrelation and ExR-PAINT correlation (calculated pixel-wise between intensity values normalized to the minimum and maximum of the image, see Methods; see Supplementary Table 1 for statistics. $n = 101$ synaptic ROIs from 5 fields of view from 3 wells of cultured neurons from 1 culture batch). **i**, Same as **h**, for ExR-ExR autocorrelation vs ExR-PAINT correlation. **j**, Estimated population distribution (violin plot of density, with a dashed line at the median and dotted lines at the quartiles) of the normalized absolute difference in radial distance between neighbouring synaptic puncta centroids (absolute value of PAINT-ExR, normalized to PAINT distance; see Supplementary Table 1 for statistics. $n = 27$ cropped synaptic pair ROIs from 5 fields of view of 30 μm × 30 μm each, 1 culture batch). **g**, Root mean square error vs measurement length (in biological units), calculated via a non-rigid registration algorithm of DNA-PAINT vs ExR-processed cultured neurons ($n = 5$ fields of view from 3 wells from 1 culture batch). Black line, mean; grey shading, standard deviation.

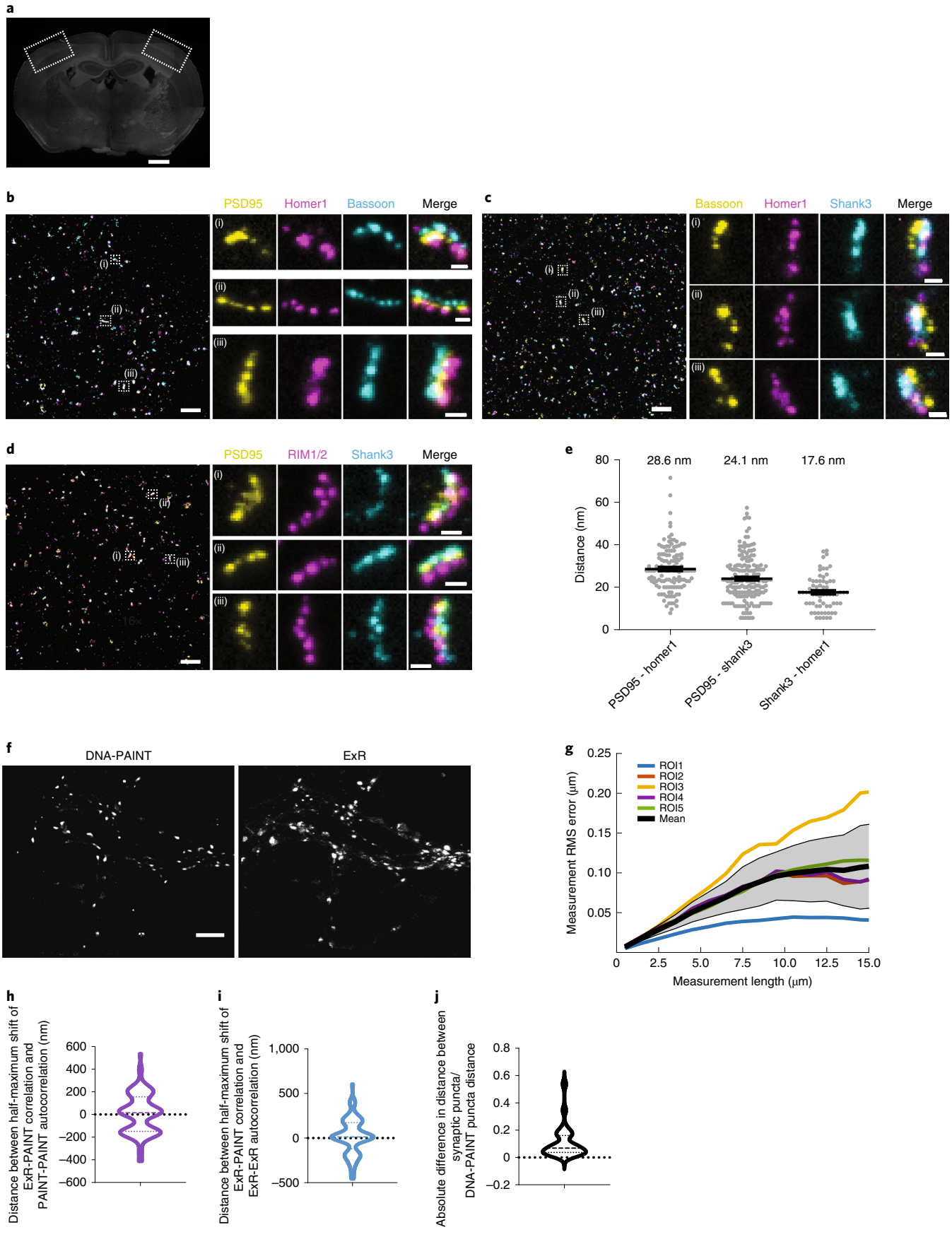
a
b
PSD95
Homer1
Bassoon
Merge
c
Bassoon
Homer1
Shank3
Merge
d
PSD95
RIM1/2
Shank3
Merge
e
28.6 nm
24.1 nm
17.6 nm
Distance (nm)
PSD95 - homer1
PSD95 - shank3
Shank3 - homer1
f
DNA-PAINT
ExR
g
ROI1
ROI2
ROI3
ROI4
ROI5
Mean
Measurement RMS error (μm)
Measurement length (μm)
h
Distance between half-maximum shift of ExR-PAINT correlation and PAINT-PAINT autocorrelation (nm)
i
Distance between half-maximum shift of ExR-PAINT correlation and ExR-ExR autocorrelation (nm)
j
Absolute difference in distance between synaptic puncta/ DNA-PAINT puncta distance

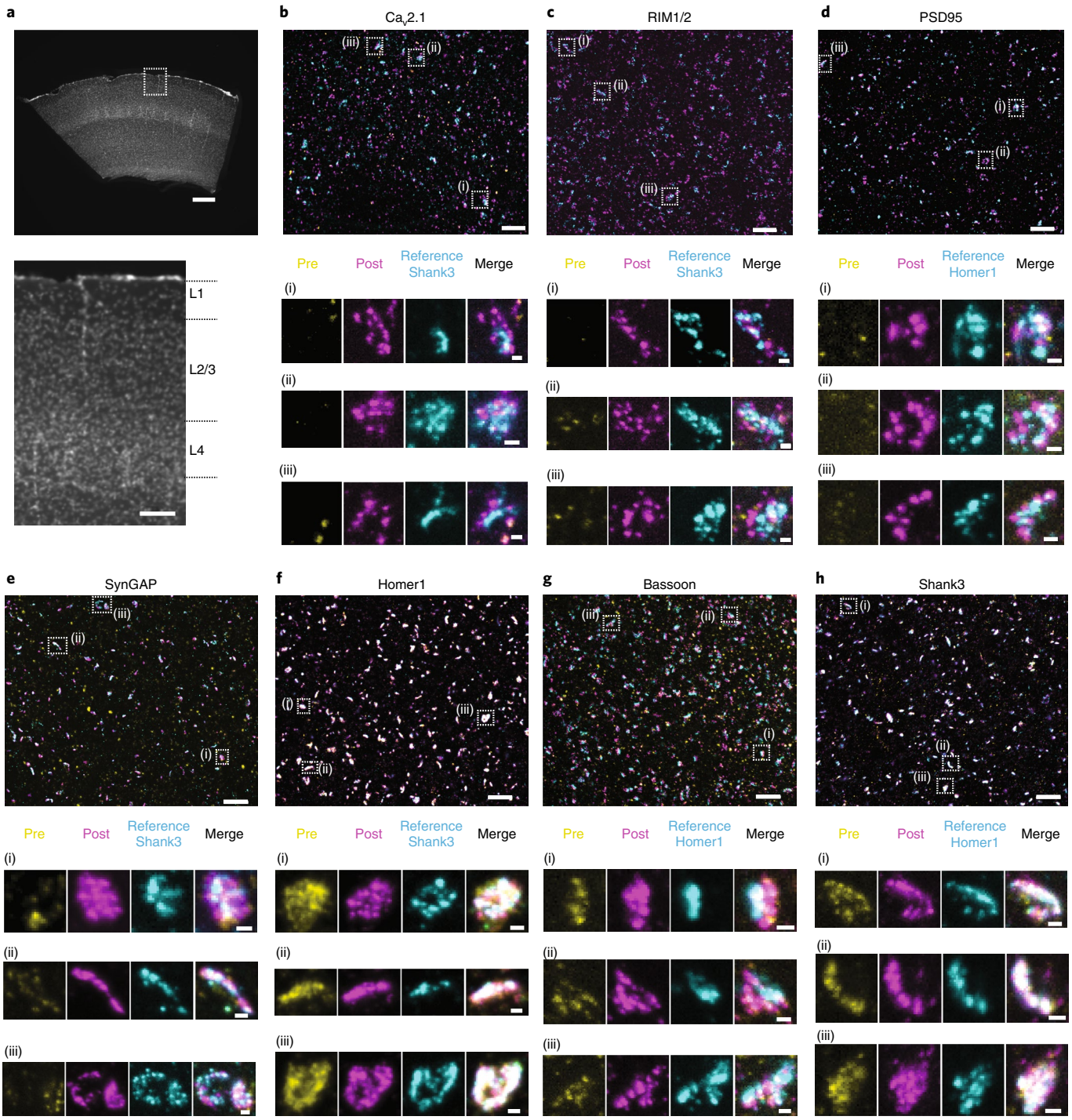

Fig. 3 | Validation of ExR enhancement and effective resolution in synapses of mouse cortex. a, Low-magnification widefield image of a mouse brain slice with DAPI staining showing somatosensory cortex (top) and zoomed-in image (bottom) of boxed region containing L1, L2/3 and L4, which are imaged and analysed after further expansion in **b**–**h**. Scale bar, 300 μm (top) and 100 μm (bottom). **b**–**h**, Confocal images of maximum intensity projections of specimen after immunostaining with antibodies against $Ca_v2.1$ (Ca^{2+} channel P/Q-type) (**b**), RIM1/2 (**c**), PSD95 (**d**), SynGAP (**e**), Homer1 (**f**), Bassoon (**g**) and Shank3 (**h**) in somatosensory cortex L2/3. For pre-expansion staining, primary and secondary antibodies were stained before expansion, the stained secondary antibodies anchored to the gel, and fluorescent tertiary antibodies applied after expansion to enable visualization of pre-expansion staining. For post-expansion staining, the same primary and secondary antibodies were applied after ExR. Antibodies against Shank3 (**b**, **c**, **e**, **f**) or Homer1 (**d**, **g**, **h**) were applied post-expansion as a reference channel. Confocal images of cortex L2/3 (top) show merged images of pre- and post-expansion staining, and the reference channel. Zoomed-in images of three regions boxed in the top image (**i**–**iii**, bottom) show separate channels of pre-expansion staining (yellow), post-expansion staining (magenta), reference staining (cyan) and merged channel. Scale bar, 1.5 μm (top); 150 nm (bottom of **i**–**iii**). Shown are images from one representative experiment from two independent replicates.

All seven proteins exhibited well-defined images when post-expansion stained, with the geometry reflecting characteristic synaptic shapes. For example, a pre-synaptic and a post-synaptic stain (Fig. 3b,c,g) revealed parallel regions with a putative synaptic cleft in between, although note that this was only visible if the synapse was being imaged from the side; if a synapse was being imaged with the axial direction of the microscope perpendicular to the synaptic cleft, then the image might look more disc-shaped[4,8,23]. In many cases, however, post-ExR staining revealed more detailed structures of synapses compared with what was visualized with pre-expansion staining—for example, calcium channels (Fig. 3b), RIM1/2 (Fig. 3c), PSD95 (Fig. 3d), SynGAP (Fig. 3e) and Bassoon (Fig. 3g) appeared more prominent post-expansion than pre-expansion. Applying a conventional antigen retrieval protocol did not result in such improvements (Supplementary Fig. 2), suggesting that the decrowding effect observed via ExR was indeed due to expansion, and not simply due to denaturation or antigen retrieval-like effects associated with other aspects of the ExR process.

To quantitate the improvement in staining enabled by ExR, we measured the amplitude and volume of each synaptic protein stain, both within and just outside of identified synapses. First, we manually identified between 49–70 synapses (see Supplementary Table 2 for exact numbers) per ~$350 \times 350 \times 20\,\mu m^3$ (in physical units, for example, what is actually seen through the microscope lens) field of view, choosing the largest and brightest synapses on the basis of reference channel staining (that is, Homer1 or Shank3). We developed an automated method to segment synaptic puncta from nearby background. Briefly, we created binary image stacks for each channel using a threshold equal to a multiple of the average measured standard deviation of five manually identified background regions (not blinded to condition), filtered three-dimensional (3D) connected components on the basis of size and used dilated reference channel ROIs to segment putative synaptic puncta (Supplementary Fig. 3 and Methods). We dilated reference channel-defined ROIs to relax the requirement of exact co-localization of pre-synaptic proteins with a post-synaptic reference. We found that post-expansion staining increased signal intensity and mean total volume of signal within dilated reference channel-defined ROIs, without meaningfully affecting background staining (that is, signal just outside the dilated reference channel-defined ROIs) (Extended Data Fig. 2a,b). In summary, all proteins except Homer1 and $Ca_v2.1$ showed significantly increased signal intensity of post-expansion staining within dilated reference ROIs, with minimal increase in the background (Extended Data Fig. 2a and Supplementary Table 3 for full statistical analysis). (We note that there was no change in signal intensity in the background for PSD95, but observed a bimodal distribution of signal intensity increases in the foreground and background due to abnormally high signal in one animal.) Similarly, all proteins except Homer1 exhibited increased total volume of post-expansion staining signals within dilated reference ROIs, and minimal or no increase in the volume of background ROIs (Extended Data Fig. 2b and Supplementary Table 4 for full statistical analysis).

Because Homer1 and Shank3 had the smallest changes in pre- vs post-expansion staining, they were chosen as reference channels to indicate the locations of putative synapses for pre- vs post-expansion test stain comparisons, as mentioned above. Different antibodies may bind to different sites on a target protein, and we found that a different antibody against PSD95 (from Cell Signaling Technology, CST3450S) from the one used in Fig. 3d (ThermoFisher, MA1-046) showed similar signal intensity and volume when compared pre- vs post-staining (Supplementary Fig. 4); perhaps, in future studies, multiple antibodies against different parts of a single protein in pre vs post-expansion comparisons could be used to gauge the density of the environment around different parts of that protein.

We further analysed synaptic protein signals pre- vs post-expansion in the context of different cortical layers. We quantified volume and signal-to-noise ratio (SNR; signal intensity divided by standard deviation of the background) of each protein in 3D synaptic structures by binarizing signals over a threshold (a multiple of the standard deviation of the intensity within a manually selected background region; see Methods) and selecting putative synapses in each ~$350 \times 350 \times 20\,\mu m^3$ field of view imaged above, comparing the values of pre- vs post-expansion staining in each layer of somatosensory cortex (L1, L2/3 and L4, respectively) (Extended Data Fig. 2c,d). Post-expansion images exhibited larger volumes and improved SNR in each layer for all synaptic proteins (see Supplementary Tables 6 and 7 for full statistics).

In previous work, we showed using the original iterative expansion microscopy (iExM) protocol, which uses pre-expansion staining, that we could achieve effective resolutions of ~20 nm with low distortion due to the expansion process[4]. As another independent way to gauge the potential distortion obtained by staining with antibodies post-expansion, we compared the shapes of synaptic puncta as seen with the pre-expansion stain, with the shapes as seen with the new post-expansion stain, using the within-sample dual staining method used in Fig. 3b–h. We compared various properties of synaptic puncta between pre- and post-expansion staining conditions, using the reference proteins Homer1 and Shank3 since they had similar intensities and volumes when comparing pre- and post-expansion datasets, and therefore might be appropriate for comparing shape features across these conditions (Extended Data Fig. 3). In summary, we did not see any substantial distortion being introduced by post-expansion staining; for example, we found no significant difference in the number of synaptic puncta when we compared pre- vs post-expansion staining in the same sample (Extended Data Fig. 2e), and when we measured the shift in puncta positions between pre- and post-stained conditions, we observed average shifts of <10 nm (in biological units, that is, physical size divided by the expansion factor) between post- and pre-expansion staining for both Homer1 and Shank3 (Extended Data Fig. 2f,g; see Supplementary Table 5 for full statistics). Thus, ExR preserves, relative to classical pre-expansion staining, the locations of proteins with high fidelity for the purposes of post-expansion staining.

Synaptic nanocolumns coordinated with calcium channel distributions. Coordinating pre- and post-synaptic protein arrangement in a nanocolumn structure which aligns molecules within the two neurons contributes to precision signalling from pre-synaptic release sites to post-synaptic receptor locations[23,24], as well as to the long-term plasticity of synaptic function[25]. Given that ExR is capable of unmasking, with nanoscale precision, synaptic proteins that are otherwise not detectable, we next sought to explore the nanocolumnar architecture of pre- and post-synaptic proteins, with a focus on important molecules that have not yet been explored in this trans-synaptic alignment context. As noted above, ExR greatly helps with visualization of calcium channels, which are among the most important molecules governing the activation of synaptic release machinery, with nanometre-scale signalling contributing to the precision of synaptic vesicle fusion. However, the nanoscale mapping of calcium channels in the context of nanocolumnar alignment in brain tissue remains difficult[26–28] (Fig. 3b). We thus applied ExR to investigate whether calcium channels occupy nanocolumns with other pre- and post-synaptic proteins, such as the critical pre- and post-synaptic proteins RIM1/2 and PSD95, respectively, across the layers of the cortex (Fig. 4a–d).

We first performed a 3D autocorrelation function ($g_a(r)$)-based test which provides information about the intensity distribution within a defined structure (see Methods). Any heterogeneity in the intensity distribution within the cluster will result in a $g_a(r) > 1$, and the distance at which the $g_a(r)$ crosses 1 can be used to estimate the size of the internal heterogeneity, here termed a nanodomain[23]. In all cortical layers, our autocorrelation analysis shows that all

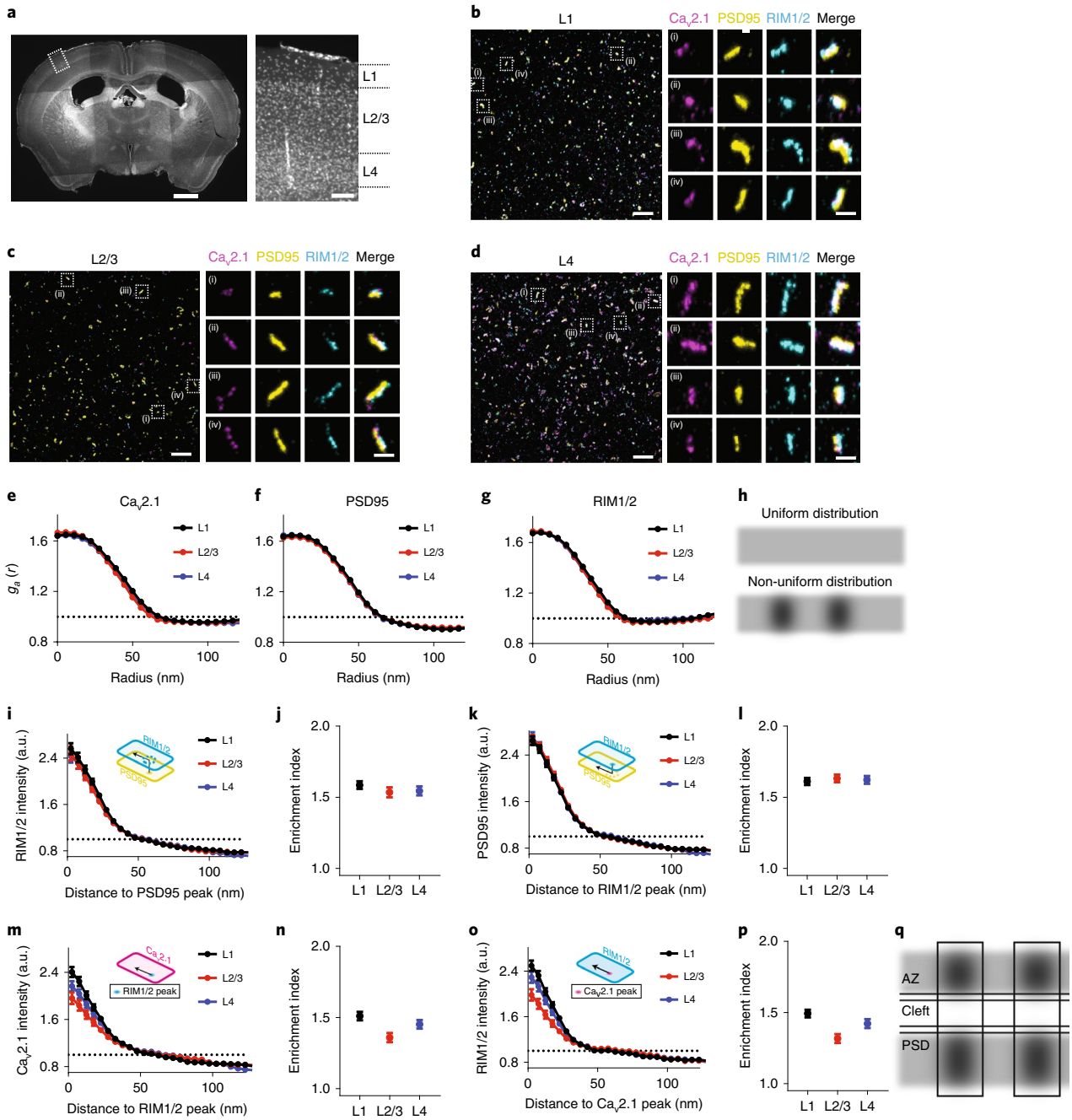

Fig. 4 | ExR reveals how calcium channel distributions participate in trans-synaptic nanoarchitecture. a, Low-magnification widefield image of DAPI-stained mouse brain slice (left) and zoomed-in view (right) of the boxed region showing layers 1–4 of the cortex. Scale bar, 1,000 μm (left) and 100 μm (right). **b**–**d**, Confocal images (maximum intensity projections) of layers 1, 2/3 and 4, respectively, after performing ExR and immunostaining with antibodies against $Ca_v2.1$ (calcium channel) (magenta), PSD95 (yellow) and RIM1/2 (cyan). Left: low-magnification images. Right: zoomed-in images of four regions (**i**–**iv**) with separated channels for each antibody along with the merged image. Scale bar, 1 μm (left) and 100 nm (right, **i**–**iv**). Shown are images from one representative experiment from two independent replicates. **e**–**g**, Autocorrelation analysis for $Ca_v2.1$ (**e**), PSD95 (**f**) and RIM1/2 (**g**) for different layers. **h**, Schematic illustration of protein distribution based on interpretation of autocorrelation results in **e**–**g**. A uniform distribution (top) would be predicted if $g_a(r) = 1$ at all radii (dotted lines in **e**–**g**), whereas a non-uniform distribution with one or more regions of high local intensity (bottom) would be predicted if $g_a(r) > 1$ at short radii and decayed as the radius is increased. **i**–**p**, Enrichment analysis that calculates the average molecular density for RIM1/2 to the PSD95 peak (**i**), PSD95 to the RIM1/2 peak (**k**), $Ca_v2.1$ to the RIM1/2 peak (**m**) and RIM1/2 to the $Ca_v2.1$ peak (**o**), with the corresponding mean enrichment indices shown in **j**, **l**, **n** and **p** (see Methods for exact *n* values). Error bars indicate s.e.m. **q**, Schematic illustration of protein distribution based on interpretation of enrichment analysis results in **i**–**p**. Enrichment values above 1 represent regions of high local intensity in the measured channel, so the enrichment profiles in **i**, **k**, **m** and **o** suggest that the peak of the reference channel closely aligns with regions of high intensity in the measured channel for each of the four comparisons. Therefore, this suggests that enriched regions of any two proteins (RIM1/2, PSD95 and $Ca_v2.1$) are aligned in nanoscale precision with each other. Calcium channels located close to vesicle fusion sites (dictated by RIM1/2) may enhance the calcium sensitivity of fusion. Additionally, post-synaptic receptors may be exposed to higher, faster peaks of neurotransmitter concentration when vesicle release sites are located directly opposite receptor nanoclusters (PSD95 being a receptor-anchoring protein). AZ, active zone; PSD, post-synaptic density.

3 proteins explored exhibited a non-uniform arrangement, forming nanodomains with average diameters of about 60–70 nm (in biological units; Fig. 4e–h). To analyse the spatial relationship between the two distributions and the average molecular density of RIM1/2, PSD95 and $Ca_v2.1$ relative to each other, we performed a protein enrichment analysis, which is a measure of volume-averaged intensity of one channel as a function of distance from the peak intensity of another channel (see Methods). To more easily compare the extent of the enrichment between these proteins in each layer, we also calculated the enrichment index, which is an average of all enrichment values within 60 nm (biological units) of the peak of a designated channel. Our analysis shows that the centres of nanodomains of RIM1/2, PSD95 and $Ca_v2.1$ are enriched with respect to each other (Fig. 4i–p).

Of particular interest, the nanoscale co-localization of $Ca_v2.1$ with RIM1/2 (and thus the vesicle site) probably minimizes the distance between the channels and the molecular Ca sensors that trigger vesicle fusion (Fig. 4q), consistent with the physiological concept of nanodomain coupling that tunes the efficacy and frequency-dependence of neurotransmission[29]. Furthermore, the precise alignment between RIM1/2 and PSD95 may reduce the diffusion distance of the released neurotransmitter before reaching post-synaptic receptors (Fig. 4q). Thus, these nanoscale arrangements may help to optimize the speed, strength and plasticity of synaptic transmission. To the best of our knowledge, the 3D nanoarchitecture of the distribution of voltage-gated calcium channels within the trans-synaptic framework in brain tissue has not been previously probed.

Periodic amyloid nanostructures in Alzheimer's model mouse brain. In addition to densely crowded proteins in healthy functioning compartments like synapses, densely crowded proteins appear in pathological states like Alzheimer's disease. Protein aggregates known as β-amyloid are thought to play roles in synaptic dysfunction, neurodegeneration and neuroinflammation[30]. However, the densely packed nature of these aggregates may make the nanoscale analysis of their ultrastructure within brain tissue difficult to understand. To understand the nanoarchitecture of β-amyloid in the cellular context of brain tissue, we applied ExR to the brains of 5xFAD Alzheimer's model mice (Fig. 5a), as this widely used animal model of Alzheimer's exhibits an aggressive amyloid pathology[31]. We employed two different commercially available antibodies for β-amyloid, 6E10 (which binds to amino acid residues 1–16 of human Aβ peptides) and 12F4 (which is reactive to the C terminus of human Aβ and has specificity towards Aβ42). We were particularly interested in investigating the relationship between amyloid deposits and white matter tracts, as these regions have been implicated in human imaging data[32–35] but are less investigated in mouse models. We previously reported the accumulation of Aβ aggregates along the fornix, the major white matter tract connecting the subiculum and mammillary body, early in disease progression[35].

We co-stained the amyloid antibodies along with the axonal marker SMI312 and compared pre-expansion staining with that obtained after ExR. Plaques appeared to be larger and to have finer-scaled features in post-expansion staining than in pre-expansion staining (Fig. 5b,c) when visualized by either 6E10 or 12F4 antibodies; thus, the post-expansion staining may unveil aspects of plaque geometry that are not easily visualized through traditional means. Additionally, post-ExR staining revealed detailed nanoclusters of β-amyloid that were not seen when staining was done pre-expansion (Fig. 5b,c). These nanodomains of β-amyloid appeared to occur in periodic structures (Fig. 5b(i–iv),c(i–iv)). Co-staining with two different β-amyloid antibodies, D54D2 (which binds to isoforms Aβ37, Aβ38, Aβ40 and Aβ42) along with 6E10 or 12F4 in ExR-processed 5xFAD fornix showed similar patterns of periodic nanostructures, which means the observed periodic nanostructures are probably not composed of specific isoforms (Extended Data Fig. 4a,b). These nanodomains, and periodic structures thereof, were not visualized through pre-expansion staining, which was also confirmed using unexpanded tissue (Extended Data Fig. 4c).

To see whether the periodic nanostructures of β-amyloid revealed through ExR were just non-specific staining artefacts of ExR, we performed ExR on wild-type (WT) mice as a control, which should not have any labelling for human β-amyloid. No β-amyloid structures were observed in ExR-processed WT brain (Supplementary Fig. 5a). Our quantitative analysis examining the volume of amyloid in ExR-processed WT and 5xFAD mice confirms that there is indeed a large amount of amyloid volume occupied in 5xFAD samples, but essentially no such volume occupied in ExR-processed WT mice (Supplementary Fig. 5b). The lack of amyloid staining in ExR-processed WT mice makes it unlikely that the staining seen in ExR-processed 5xFAD mouse brain is non-specific. Applying a conventional antigen retrieval protocol recovered some amyloid staining, but less than by ExR (Supplementary Fig. 6), suggesting that the decrowding effect observed via ExR was indeed due to expansion and not simply due to denaturation or antigen retrieval-like effects associated with other aspects of the ExR process. The intact staining of axonal and myelin markers (Fig. 6 and Extended Data Fig. 5) adjacent to the amyloid puncta highlight how, within the same volume of tissue, some structures can exhibit periodicity while others remain smooth and continuous, highlighting the small length scales over which the architecture of nanostructures is regulated in cells and tissues.

Co-clustering of amyloid nanodomains and ion channels. To understand the biological context of these periodic Aβ nanostructures, we stained brain slices with antibodies against the ion channels Nav1.6 and Kv7.2. Alzheimer's disease is associated with altered neuronal excitability and alterations in ion channels[36]. We stained ExR-processed 5xFAD fornix-containing brain slices with antibodies against potassium channels (Kv7.2) and against β-amyloid (12F4) (Fig. 6a and Supplementary Fig. 7a). The periodic β-amyloid nanostructures co-localized with periodic nanoclusters of potassium channels. In ExR-processed WT fornix, such β-amyloid clusters and frequent clusters of potassium or sodium channel staining were not found (Supplementary Fig. 7b,c). Co-staining of β-amyloid (12F4) and sodium channels (Nav1.6) showed co-localization as well (Fig. 6b and Supplementary Fig. 7d). Specifically, over half of β-amyloid nanoclusters co-localized with Nav1.6 (Supplementary Fig. 7d(i)), and within these co-localized regions, Nav1.6 puncta were much smaller than β-amyloid nanoclusters (Supplementary Fig. 7d(ii)). We also found other interesting amyloid patterns, such as helical structures along axons (Fig. 6b).

To probe the periodic amyloid/Kv7.2 patterns further, we obtained a cross-sectional profile of a stretch of axon, showing that Aβ42 (magenta) and Kv7.2 (yellow) were highly overlapping and had similar periodicities (Fig. 6c). A further histogram analysis showed the periodicity of both repeated protein structures to be 500–1,000 nm (Fig. 6d), which we confirmed by Fourier analysis (Fig. 6e,f). This periodicity is notably higher in spatial frequency, by orders of magnitude, than the inter-node-of-Ranvier distances of brain white matter, which range from 20–100 μm[37–39].

Our analysis along individual segments of axons showed that a high fraction of Aβ42 clusters contained Kv7.2 clusters (Fig. 6g), a result that we confirmed by measuring the distance between the centroids of overlapping Aβ42 and Kv7.2 nanoclusters, finding extremely tight co-localization within a few tens of nanometres (Fig. 6h). Median sizes of nanoclusters were around 150 nm for both Aβ42 and Kv7.2 (Fig. 6i); indeed, overlapping nanodomains of Aβ42 and Kv7.2 were highly correlated in size (Fig. 6j), suggesting a potential linkage between how they are formed and organized as multiprotein complexes.

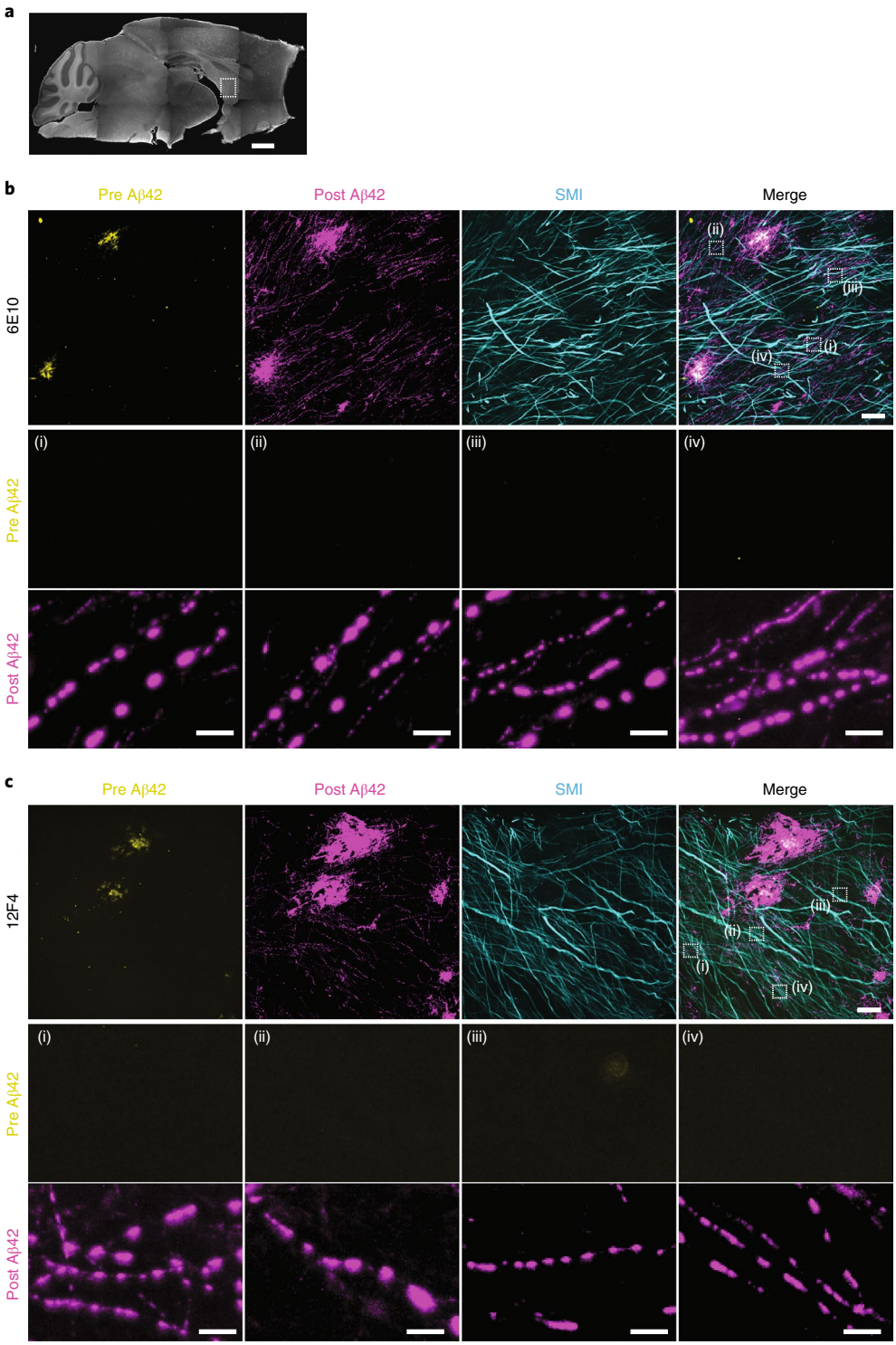

Fig. 5 | ExR reveals periodic nanoclusters of Aβ42 peptide in the fornix of Alzheimer's model 5xFAD mice. a, Epifluorescence image showing a sagittal section of a 5xFAD mouse brain with the fornix highlighted (dotted box). Scale bar, 1,000 μm. **b**,**c**, Top row: ExR confocal images (maximum intensity projections) showing immunolabelling against Aβ42 peptide with two different monoclonal antibodies 6E10 (**b**) and 12F4 (**c**). From left to right: pre-expansion immunolabelling of Aβ42 (yellow), post-expansion labelling of Aβ42 (magenta), post-expansion SMI (neurofilament protein), and merged pre- and post-expansion staining of Aβ42 with post-expansion staining of SMI. Middle and bottom rows: insets (**i**–**iv**) showing the regions of interest highlighted (dotted boxes) in the merged images in the top rightmost panels of **b** anc **c**; middle row: pre-expansion Aβ42 labelling; bottom row: post-expansion Aβ42 labelling. Post-ExR staining reveals periodic nanostructures of β-amyloid, whereas pre-expansion staining can detect only large plaque centres. Scale bar, 10 μm (top); 1 μm (bottom, **i**–**iv**).

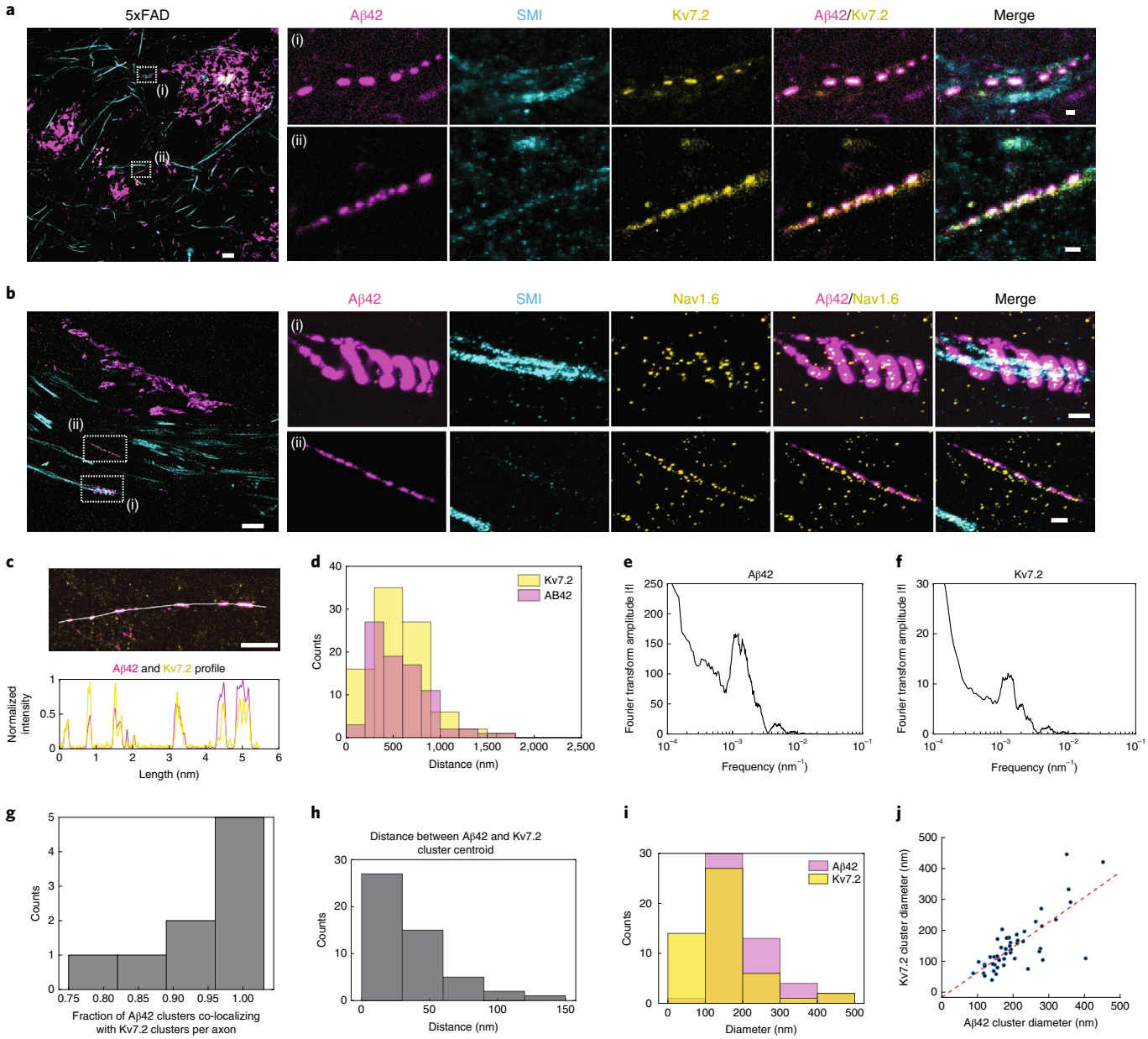

Fig. 6 | ExR reveals co-localized clusters of Aβ42 peptide with potassium and sodium ion channels in the fornix of Alzheimer's model 5xFAD mice. **a**,**b**, ExR confocal image (maximum intensity projections) showing post-expansion Aβ42 (magenta), SMI (cyan) and Kv7.2 (yellow) staining (**a**), and Aβ42 (magenta), SMI (cyan) and Nav1.6 (yellow) staining (**b**) in the fornix of a 5xFAD mouse. Leftmost panel, merged low-magnification image. Scale bar, 4 μm. Insets (**i**,**ii**) show close-up views of the boxed regions in the leftmost image for Aβ42, SMI, Kv7.2, Aβ42-Kv7.2 merged and Aβ42-Kv7.2-SMI merged, respectively (**a**), and Aβ42, SMI, Nav1.6, Aβ42-Nav1.6 merged and Aβ42-Nav1.6-SMI merged, respectively (**b**). Scale bar, 400 nm; $n = 5$ fields of view from two slices from two mice. **c**, ExR confocal image (maximum intensity projections) showing Aβ42 (magenta) and Kv7.2 (yellow) clusters in a 5xFAD mouse (top) with the indicated cross-section profile shown (bottom). Scale bar, 1 μm. Shown are images from one representative experiment from four independent replicates. **d**, Histograms showing distances between adjacent Aβ42 (magenta) and Kv7.2 (yellow) clusters in 5xFAD mice along imaged segments of axons ($n = 97$ Aβ42 clusters, 92 Kv7.2 clusters from 9 axonal segments from 2 mice). **e**,**f**, Fourier-transformed plots of Aβ42 (**e**) and Kv7.2 (**f**) showing the same peak position (from the same dataset as in **d**). **g**, Histogram showing the fraction of Aβ42 clusters co-localizing with Kv7.2 clusters along individual segments of axons ($n = 50$ cluster pairs from 9 axonal segments from 2 mice). **h**, Histogram showing the distance between the centroids of co-localized Aβ42 and Kv7.2 clusters (same dataset as in **d**). **i**, Histograms showing the diameters of Aβ42 clusters (magenta) and Kv7.2 clusters (yellow) ($n = 50$ cluster pairs from 9 axonal segments from 2 mice). **j**, Scatterplot showing the diameters of co-localized Aβ42 and Kv7.2 clusters. Red line, y = x, for reference.

To facilitate visualization of the 3D shapes of these Aβ42 and Kv7.2 puncta, we show three orthogonal slices in the *x*-*y*, *x*-*z* and *y*-*z* planes (*x*- and *y*-directions being transverse directions, and the *z*-direction being axial) that intersect the centre of each puncta. Qualitatively, we observed that the majority of these puncta are oblong, with smooth continuous Aβ42 ellipsoids and more punctate Kv7.2 puncta, with some (but not all) Kv7.2 puncta being found within Aβ42 puncta. A larger volume of Aβ42 (as a fraction of total Aβ42 puncta volume) was found inside Kv7.2 puncta compared with the fraction of Kv7.2 volume found inside Aβ42 puncta (Fig. 7 and

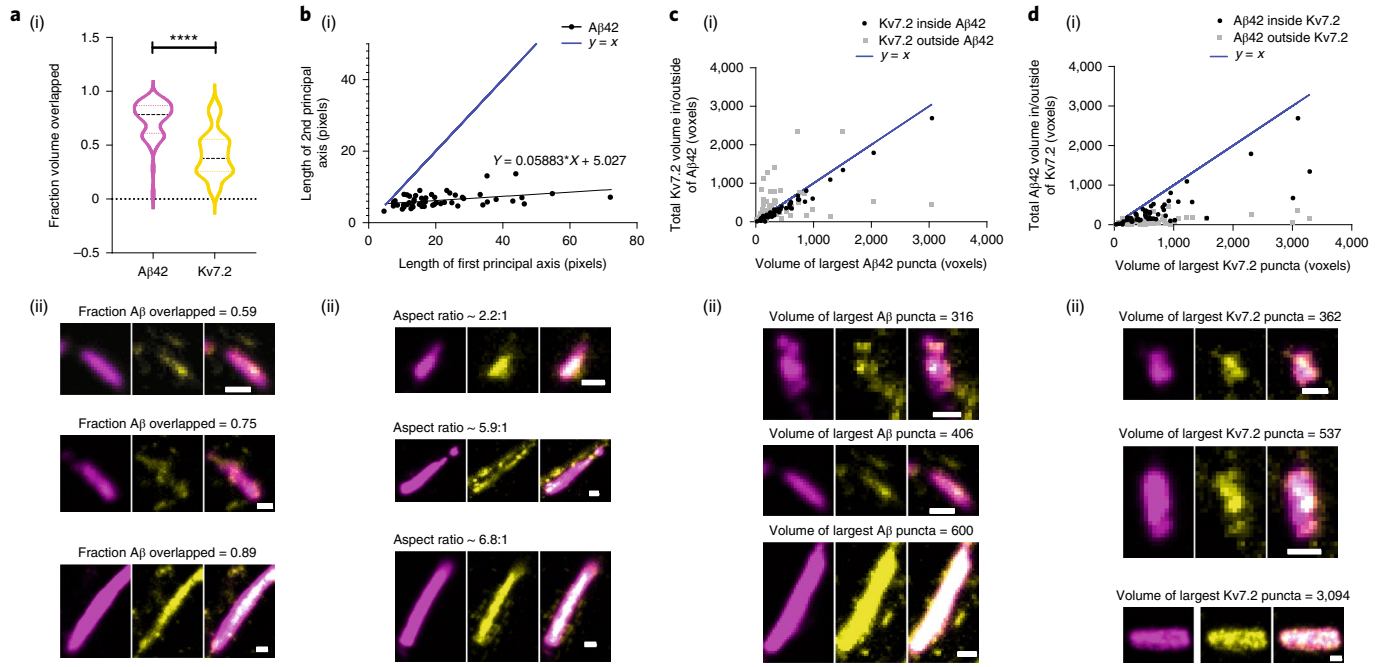

Fig. 7 | Analysis of Aβ42 peptide and potassium ion channel nanoclusters in shapes and their relationships. a, (**i**) Fraction of total Aβ42 and Kv7.2 puncta volume overlapped with one another in cropped Aβ42 clusters ($n = 55$ clusters from 2 5xFAD mice; $P < 0.0001$, two-sided pairwise t-test). ****$P < 0.0001$. (**ii**) Representative images illustrating the difference in the proportion of mutually overlapped volume between Aβ42 and Kv7.2 as a fraction of total Aβ42 or Kv7.2 volume. Scale bar, 100 nm. **b**, (**i**) Length of the second principal axis of the ellipsoid that has the same normalized second central moments as the largest Aβ42 punctum in an ROI, vs the length of the first principal axis of this ellipsoid (in pixels, 1 pixel = 11.44 nm in x- and y-directions (transverse) and 26.67 nm in the z-direction (axial); black points represent individual manually cropped ROIs; slope of best-fit line from simple linear regression =0.05883, $P = 0.0020$, $F = 10.59$, d.f. = 53). Compare to the line $y = x$ (blue). (**ii**) Representative images illustrating the oblong shape of Aβ42 puncta for three first principal axis lengths: shorter (top row), medium (middle row) and longer (bottom row). While the length of the first principal axis varies significantly between these examples, the length of the second principal axis remains similar among the three clusters. **c**, (**i**) Total volume (in voxels, 1 voxel = 11.44 × 11.44 × 26.67 or 3,490 nm^3) of Kv7.2 puncta overlapped/inside (black, $R^2 = 0.980$, $P < 0.0001$) and outside (grey, $R^2 = 0.0582$, $P = 0.0979$) Aβ42 puncta as a function of the volume of the largest Aβ42 puncta within an ROI, compared to the line $y = x$ (blue). (**ii**) Representative images illustrating that the volume of Kv7.2 outside of Aβ42 is relatively constant as Aβ42 puncta size increases. As in **b**(**ii**), the three clusters shown are ordered by increasing size. **d**, (**i**) The converse of **c**: total volume of Aβ42 puncta overlapped/inside (black, $R^2 = 0.6531$, $P < 0.0001$) and outside (grey, $R^2 = 0.1876$, $P = 0.0010$) of Kv7.2 puncta as a function of the volume of the largest Kv7.2 puncta within an ROI, compared to the line $y = x$ (blue). (**ii**) Representative images illustrating that the volume of Aβ42 outside of Kv7.2 is smaller than the volume of Aβ42 co-localized with Kv7.2, and both values are positively correlated with the volume of the largest Kv7.2 puncta. Scale bar (**a**(**ii**)-**d**(**ii**)), 100 nm. Shown are images from one representative experiment from four independent replicates.

Supplementary Fig. 8a). On average, the mean volume of an Aβ42 puncta was slightly larger than that of a Kv7.2 puncta (Supplementary Fig. 8b, paired t-test, $P = 0.0001$, $t = 4.116$, d.f. = 54). Quantification of shape characteristics confirmed these observations and revealed more subtle patterns. Representative images illustrating the observed trends are shown in Fig. 7a(ii)–d(ii). Despite the larger volume of Aβ42 puncta, the fraction of Aβ42 volume mutually overlapped with (inside of) Kv7.2 puncta was larger than the fraction of Kv7.2 mutually overlapped with (inside of) Aβ42 puncta (Fig. 7a; $P < 0.0001$, $t = 10.94$, d.f. = 54). When considering the ellipsoidal shapes of these puncta, the relationship between the second and first principal axis lengths was highly sublinear (Fig. 7b), and the average aspect ratio (ratio of first to second principal axis length) was ~3.5:1 (mean 3.464, standard deviation 1.911, $n = 55$ puncta), indicating a highly oblong shape (slope of best-fit line from simple linear regression =0.05883, $P = 0.0020$, $F = 10.59$, d.f. = 53). While the number of Kv7.2 present in each manually cropped ROI was not correlated with the volume of the largest Aβ42 puncta within the cropped ROI (Supplementary Fig. 8c; simple linear regression, 95% CI of slope (−0.003940, 0.005947)), the mean Kv7.2 puncta volume was significantly correlated with the mean Aβ42 puncta volume (Supplementary Fig. 8d; simple linear regression, 95% CI of slope (0.09878, 0.2437), $R^2 = 0.2977$, $P < 0.0001$, $F = 22.47$, d.f. = 53). Thus, as the size of Aβ42 aggregates increases, Kv7.2 aggregates also increase in size, but not in number. We found that the volume of Kv7.2 puncta inside Aβ42 puncta is highly correlated with the volume of the Aβ42 puncta (Fig. 7c; simple linear regression, 95% CI of slope (0.8353, 9037), $R^2 = 0.98$, $P < 0.0001$, $F = 2{,}593$, d.f. = 53), but the volume of Kv7.2 puncta outside of Aβ42 puncta is not correlated with Aβ42 puncta volume (Fig. 7c; simple linear regression, 95% CI of slope (−0.03919, 0.4503), $R^2 = 0.05082$, $P = 0.0929$, $F = 2.838$, d.f. = 53). Conversely, the total volume of Aβ42 puncta inside of Kv7.2 puncta was not as strongly correlated with the volume of the largest Kv7.2 puncta (Fig. 7d; simple linear regression, 95% CI of slope (0.4198, 0.6307), $R^2 = 0.6531$, $P < 0.0001$, $F = 99.29$, d.f. = 53) in the cropped ROI. The volume of Aβ42 puncta outside of Kv7.2 was weakly but significantly correlated with the size of the largest Kv7.2 puncta (Fig. 7d; 95% CI of slope (0.0250, 0.09245) $R^2 = 0.1876$, $P = 0.0010$, $F = 12.24$, d.f. = 53). Finally, we found that the non-overlapped volume as a function of overlapped volume was much larger on average for Kv7.2 than for Aβ42 (Supplementary Fig. 8e; paired t-test, $P < 0.0001$, $t = 5.985$, d.f. = 54). Taken together, these results show that Kv7.2 and Aβ42 puncta are correlated in size only when physically co-localized in a tightly registered fashion, perhaps pointing to new potential hypothesized mechanisms of aggregation.

In myelinated axons, Kv7 potassium channels and voltage-gated sodium (Na_v) channels co-localize tightly with nodes of Ranvier periodically along axons[40]. We investigated whether the distribution of β-amyloid is related to the myelination state of the axons. In 5xFAD mouse fornix, myelin proteolipid protein (PLP) staining was intact and partly overlapped with both SMI and Aβ42 clusters (Extended Data Fig. 5a), with the PLP-SMI relationship being similar to that between PLP and SMI in WT animals (Extended Data Fig. 5b). Quantification of both PLP and SMI in Aβ42+ axons did not show major changes in either SMI or PLP staining intensity as a function of Aβ42 presence (Extended Data Fig. 5c).

While the biological relevance of this periodicity and co-localization of β-amyloid with Kv7.2 and Nav1.6 needs further investigation, it is interesting to note that Nav1.6 and Kv7.2 ion channels can regulate neural excitability[41–43], and Aβ peptides have also been known to influence excitability[44]. As these Aβ structures were often, although not always, co-localized with SMI-positive axons and are highly reactive for Aβ42, we interpret these structures as periodic amyloid depositions. In the future, it will be interesting to see whether these structures play direct roles in neural hyperexcitability in Alzheimer's. It is curious to reflect here that periodicity and order[45–55] are often thought of as associated with healthy biological systems whose functionality may be supported by such crystallinity. On the other hand, disorder, misalignments and misfoldings are often tied to pathological states. Here we find a curious mixture of the two—a periodicity that seems to be associated with a pathological state and may have implications for new hypotheses related to Alzheimer's pathology. We are excited to see how ExR might reveal many kinds of previously invisible nanopatterns in healthy and disease states due to its ease of use and applicability to multiple contexts, as seen here.

Discussion

The ability to optically study the crowded and complex 3D molecular nanoarchitecture of cells and tissues, such as in brain tissue, is challenging because optical super-resolution methods visualize fluorescent tags (such as antibodies) that are bound to target biomolecules, and these tags may not be able to access all the biomolecules within a nanostructure. Here we present ExR, a new expansion microscopy method that reveals previously invisible biological nanostructures by enabling 20 nm resolution imaging and protein decrowding. ExR leverages the spatial expansion property of expansion microscopy[2,3] and the 20 nm resolution of iterative expansion[4] to physically decrowd densely packed biomolecules, providing conventional antibodies with better access to epitopes, revealing more detailed and even previously unseen structures when compared with pre-expansion staining, including in intact tissues.

While many expansion papers have mentioned or implied decrowding[6,56–59], previous claims have not been accompanied with systematic data demonstrating specificity of signal-to-noise increase in specific biological structures vs background, minimal distortion between pre- and post-expansion staining, and/or whether decrowding vs heat-mediated antigen retrieval is the dominant contributor to improved staining. Nevertheless, these pioneering efforts are exciting. For example, ultrastructure expansion microscopy (U-ExM)[58] combined with confocal microscopy showed higher labelling efficiency than in unexpanded direct stochastic optical reconstruction microscopy (dSTORM) images. Indeed, the authors noted inhomogeneous tubulin signal "probably because of epitope masking of antibodies" and in the discussion, stated that the relatively smaller antibody size in post-expansion labelling approaches "unveiled" the chirality of the centriole. As another example, a previously described method that combines post-expansion staining with single-molecule localization microscopy (Ex-SMLM)[59] also claimed that expansion of the sample increases epitope accessibility and labelling efficiency. As with U-ExM, the authors claim that post-expansion staining "increases epitope accessibility and thus labelling efficiency". Here we showed, in comparisons of pre- and post-expansion staining in the same samples of brain tissue, that epitopes were indeed unmasked using ExR. We showed that the decrowding effect is not due to increases in non-specific signal or antigen retrieval effects, and that ExR does not introduce any substantial distortion relative to the non-expansion super-resolution technique DNA-PAINT.

By comparing pre- and post-expansion staining, we found that enhanced post-expansion staining is observed within synaptic structures without a corresponding increase in non-specific background staining, and preserves protein labelling abundance and localization with low distortion (<10 nm). ExR revealed biological structures, such as previously undescribed nanoscale arrangements of calcium channels within trans-synaptic nanocolumns[23] and periodic amyloid nanostructures co-clustering with ion channels in a model of Alzheimer's disease. Pre-synaptic functional diversity is maintained in part by how calcium channels are organized with respect to vesicle-resident sensor proteins that mediate calcium-fusion coupling, yet dense active-zone complexes have been difficult to map accurately in mammalian brain. The clustering of calcium channels in nanocolumns as we have observed here probably represents just one of many unique organizations of these ion channels to be discovered. The discovery of a unique pattern of periodic depositions of ion channels in amyloid aggregates in Alzheimer's disease mouse model brains is another example of the unexpected observations that can be made using this tool. Observing the distribution of ion channels in axons ex vivo has been hindered by the crowded nature of axon tracts, and these results have implications for both saltatory conduction in vivo and the mechanisms of hyperexcitability in Alzheimer's disease. We thus expect ExR to open up opportunities to observe new, previously unidentifiable biological structures via decrowding, which cannot be obtained by other super-resolution techniques.

Going forward, because ExR is an iterative expansion technique, it may be possible to achieve 100× expansion with one more round of re-embedding and gelation to obtain even better resolution and potentially single-molecule localization. Furthermore, ExR could in principle be combined with RNA fluorescence in situ hybridization (FISH), as in expansion FISH (ExFISH)[60], to label both proteins and RNA molecules, enabling visualization of the precise geometry and spatial relationship between RNA and proteins. Finally, because ExR anchors endogenous proteins to the gel, repeated rounds of antibody staining and stripping could in principle be performed, facilitating highly multiplexed imaging of potentially hundreds of proteins in the same field of view. Multiplexed ExR could in principle be used to create high-dimensional protein-protein co-localization maps, potentially revealing complex putative interactions and biological states that cannot be captured with imaging of only a few proteins at once (for example, through conventional three-colour staining and imaging). Thus, we anticipate that ExR will facilitate discoveries in biology and medicine.

Methods

Brain-tissue preparation. All procedures involving animals were in accordance with the US National Institutes of Health Guide for the Care and Use of Laboratory Animals and approved by the Massachusetts Institute of Technology Committee on Animal Care. Both male and female wild-type mice (C57BL/6 or Thy1-YFP, 6–8 weeks of age, from JAX) and 5xFAD mice (12–13 months of age, from the Mutant Mouse Resource and Research Center) were used because of the current study's focus on developing and validating a technology. Mice were deeply anaesthetized using isoflurane in room air. Mice were transcardially perfused at room temperature with ice-cold 10 ml 2% (w/v) acrylamide in phosphate buffered saline (PBS), followed by ice-cold 10 ml 30% acrylamide (w/v) and 4% paraformaldehyde in PBS. Brains were collected and incubated in 20 ml of the same fixative solution (30% acrylamide and 4% paraformaldehyde in PBS) at 4 °C overnight. Fixed brains were transferred to 100 mM glycine at 4 °C for 6 h, then stored in PBS at 4 °C for long-term storage or sectioned to 50–100-μm-thick slices with a vibrating microtome (Leica VT1000S).

Cultured-neuron preparation. Cultured mouse hippocampal neurons were prepared from postnatal ~day 0 Swiss Webster mice (Taconic) (both male and female mice were used) as previously described[61]. In summary, imaging chambers (112358 CS16-CultureWell removable chambered coverglass, Grace Bio-Lab) were pre-treated with diluted Matrigel, and 5,000–10,000 cells were plated in each well. Neurons were grown at 37 °C and 5% CO_2 in a humidified atmosphere for 14 d before fixation. The cells were also briefly washed with 1x PBS warmed to 37 °C before fixation. The cultured cells were then fixed with 4% paraformaldehyde (PFA) in 1x PBS for 10 min at room temperature. Immediately thereafter, the fixation solution was replaced with a solution of 0.7% PFA, 1% acrylamide in 1x PBS, and the samples were incubated at 37 °C for 6 h. Once incubation was done, samples were washed with 1x PBS. Samples were stored at 4 °C overnight. Before expansion, the coverglass from the cell culture well was separated using the coverglass removal tool (103259, Grace Bio-Lab).

Expansion of brain-tissue slices and cultured neurons. For the first gelling step, brain slices or cultured neurons were incubated in the first gelling solution (8.625% (w/v) sodium acrylate, 2.5% (w/v) acrylamide, 0.075% (w/v) *N*,*N*'-methylenebisacrylamide (Bis), 0.2% (w/v) ammonium persulfate initiator, 0.2% (w/v) tetramethylethylenediamine (TEMED) accelerator and 0.2% (w/v) 0.01% 4-Hydroxy-TEMPO) for 30 min at 4 °C. Slices were embedded in 4-well dish gelling chambers on coverglasses surrounded by excess first gelling solution, and incubated at 37 °C for 2 h. Cultured neurons were incubated in the first gelling solution with coverglass on top at 37 °C for 2 h. After the incubation, gels containing the tissue or cultured neurons were cut out from the chamber and incubated with denaturation buffer (200 mM SDS, 200 mM NaCl and 50 mM Tris pH 9)[5] for 1 h at 95 °C. Denatured gels were fully expanded via 4 washes for 15 min each with 5 ml distilled (DI) water in a 6-well plate.

For the re-embedding step, expanded first gels were incubated in re-embedding solution (13.75% (w/v) acrylamide, 0.038% (w/v) Bis, 0.025% (w/v) ammonium persulfate, 0.025% (w/v) TEMED) twice, replacing the first solution with freshly made re-embedding solution for 1 h each time on a shaker at room temperature. The re-embedded gels were transferred to a 4-well dish gelling chamber on coverglasses with a coverglass on top. The gelling chambers were placed in a ziplock bag with nitrogen flushing for 5 min and incubated for 2 h at 45 °C. The re-embedded gels were washed 3 times for 15 min each with 5 ml PBS in a 6-well plate.

For the third gelling step, the re-embedded gels were incubated in third gelling solution (8.625% (w/v) sodium acrylate, 2.5% (w/v) acrylamide, 0.038% (w/v) Bis, 0.025% ammonium persulfate, 0.025% (w/v) TEMED) twice, replacing the first solution with freshly made third gelling solution for 1 h each time on a shaker at room temperature. The third gels were placed in a 4-well dish gelling chamber on coverglasses with a coverglass on top. The gelling chambers were placed in a ziplock bag with nitrogen flushing for 5 min and incubated at 60 °C for 1 h.

Gels were fully expanded in DI water by changing excess water five times for 2 h each and trimming axially to reduce thickness to 1 mm to facilitate subsequent immunostaining and imaging.

Immunostaining of expanded tissues and cultured neurons. Expanded gels were incubated in blocking solution (0.5% Triton X-100, 5% normal donkey serum (NDS) in PBS) for 2 h at room temperature. Gels were then incubated with primary antibodies (see Methods Antibody list) in '0.25T' blocking buffer (0.25% Triton X-100, 5% NDS in PBS) overnight at 4 °C. Gels were washed in washing buffer (0.1% Triton X-100 in PBS) six times for 1 h each time on a shaker at room temperature. Gels were then incubated with secondary antibodies in blocking solution overnight at 4 °C, and washed in washing buffer six times for 1 h each on a shaker at room temperature. ExR-processed sample images were acquired using a Nikon CSU-W1 confocal microscope with 100% laser power and 1 s exposure time. *Z*-steps are varied between 0.250 and 0.500 µm.

Super-resolution imaging (DNA-PAINT). *Antibody conjugation.* The antibody (Jackson ImmunoResearch Laboratories, 711–005–152) was conjugated with thiolated DNA following the published protocol[62]. Briefly, 250 µM 5' thiol-modified DNA oligonucleotides were reduced by 100 mM dithiothreitol in 1× PBS + 1 mM EDTA for 1 h at room temperature. Then, excess dithiothreitol was removed using NAP5 columns (GE Healthcare Life Sciences, 17-0853-02). Carrier-free antibody (without BSA or sodium azide) formulated in 1× PBS was concentrated to 2 mg ml^{-1} using 50 KDa Amicon Ultra filters (EMDMillipore, UFC505096). Then, crosslinkers (PEGylated SMCC crosslinker, ThermoFisher, A35397) were added to an antibody tube at a 5:1 molar ratio (crosslinker:antibody) and reacted for 2 h at 4 °C. Next, antibody was purified using 0.5 ml 7 kDa Zeba desalting columns (LifeTechnologies, 89883) to remove excess crosslinker. Reduced thiol-DNA oligonucleotide was then mixed with antibody at a 5:1 molar ratio (DNA:antibody) and reacted overnight at 4 °C. Final conjugated antibodies were washed five times with 1× PBS (100 ug ml^{-1}) in Amicon Ultra filters (50k) to remove unreacted DNA oligonucleotides. Conjugated antibody was kept at 4 °C until use.

DNA sequences (5' to 3'): /5ThioMC6-D/ATACATCT (ID, Docking; Integrated DNA Technologies); AGATGTAT /Atto-655/ (ID, Imager; Biosynthesis).

Immunostaining. Neuron cultures were blocked and permeabilized in 0.1% Triton X-100, 0.1% Tween20, 3% IgG-free BSA and 5% NDS for 2 h at room temperature. Cell cultures were incubated with primary antibodies (diluted in 0.1% Triton X-100, 0.1% Tween20, 3% IgG-free BSA) overnight at 4 °C, and washed with 0.1% Tween20 and 1% IgG-free BSA five times (10 min each). Secondary antibodies were diluted in 0.1% Triton X-100, 0.1% Tween20 and 3% IgG-free BSA, incubated with samples for 2 h at room temperature and then washed as for primary antibodies. A 1:100 dilution of 100 nm gold nanoparticles (753688-25ML, Sigma-Aldrich) was then added to wells and gently spun down in a centrifuge (500 *g*, 5 min). Finally, the cells were briefly washed three times with 1× PBS + 500 mM NaCl.

DNA-PAINT. Super-resolution imaging was accomplished on a Nikon Eclipse Ti microscope that was (1) operated by Nikon Elements software, (2) used a 1.49 NA CFI Apo ×100 objective, (3) had a perfect focus system and (4) had a total internal reflection fluorescence (TIRF) laser (488 nm, 561 nm, 647 nm). Lasers were operated in TIRF mode for all acquisitions. For image acquisition, an electron multiplying (EM) charge coupled device (iXon X3 DU-897, Andor Technologies) was used. Cameras were operated at 5 MHz refresh rate with 100 EM again and a 50 ms exposure time. A ×1.5 lens was introduced into the optical path allowed for imaging, with a pixel size of 110 nm. Images were acquired using RAM capture via Nikon Fast Timelapse acquisition. Frames (15,000–20,000) of single-molecule image stacks were then acquired and analysed in Picasso. To correct for image drift, 100 nm gold nanoparticles were used as fiducial markers in the imaging process. DNA imager stock solution was diluted and used in 1× PBS + 500 mM NaCl at a working concentration of 2 nM.

Decrowding experiments. *Nanoscale-resolution imaging of synapses in somatosensory cortex.* For pre-expansion antibody staining (Fig. 3b–h), brain slices were incubated with primary antibodies in blocking solution overnight at 4 °C. Stained tissues were washed in washing buffer six times for 1 h each time on a shaker at room temperature. Secondary antibodies (100 µl, 1 mg ml^{-1}) were incubated with 6-((acryloyl)amino)hexanoic acid and succinimidyl ester (AcX) (2 µl, 1 mg ml^{-1}) overnight at room temperature to prepare AcX-conjugated secondary antibodies. Primary antibody-stained tissues were then incubated with AcX-secondary antibodies in blocking solution overnight at 4 °C and washed in washing buffer six times for 1 h each time on a shaker at room temperature. Tissue expansion was carried out as previously described. The tertiary antibodies were stained after expansion to bind against AcX-secondary antibodies to visualize the pre-expansion staining.

For post-expansion antibody staining, expanded gels were incubated with the same primary and secondary antibodies without AcX conjugation. Antibodies against Shank3 or Homer1 were provided as a reference channel after expansion.

Quantification and validation of the decrowding effect. *Comparison of ExR and DNA-PAINT synapsin staining in cultured neurons.* Two-dimensional DNA-PAINT images (Fig. 2h,i) were rendered using Picasso in Python[63] using a blur width of 0.0, oversampling of 4.74–5.42 (corresponding to a pixel resolution of 20.31–21.10 nm per /pixel), and maximum density of 350. The oversampling parameter was calculated on a per-well basis to match the pixel resolution given by the measured expansion factor of 7.7–8.0X for ExR images. The expansion factor for each well was calculated by measuring the distances between identical pairs of synapsin puncta in pre- and post-expansion images and dividing the physical units in the post-expansion image by the physical units in the pre-expansion image. The mean value over five such distances was calculated: 7.9X for well 1, 7.7X for well 2 and 8.0X for well 3. Post-expansion ExR stacks were background subtracted using Fiji's Rolling Ball algorithm with radius 50 pixels and collapsed to two dimensions using a maximum intensity projection. DNA-PAINT and ExR images were registered using custom MATLAB scripts employing automatic intensity-based rigid body registration. Images were first minimum-maximum normalized, passed through a 2D Gaussian filter (sigma = 5) and binarized using Otsu's thresholding method (MATLAB's 'graythresh'). The geometric transform was estimated using MATLAB's configurations for multimodal intensity-based registration, with the following optimizer parameters: initial radius, 0.004; epsilon, 1.5×10^{-4}; growth factor, 1.01; maximum iterations, 300. An initial rigid body transformation was estimated before calculation of the final transform using the same parameters.

To assess the accuracy/resolution and distortion of ExR compared to DNA-PAINT, we calculated linear distortion of nanoscale synaptic puncta, the difference in pairwise distances between neighbouring synaptic puncta and the differences in mean synaptic puncta number in identical cultured-neuron samples imaged using the two technologies. To analyse nanoscale error introduced by ExR relative to DNA-PAINT, ROIs containing single synaptic puncta were manually segmented from DNA-PAINT and corresponding ExR images taken from the same fields of view in the same specimens. Pixel intensity was minimum-maximum normalized separately for ExR and DNA-PAINT channels. Manually cropped individual synaptic ROIs from ExR images were automatically registered to their DNA-PAINT counterparts (note: after the global registration) using a rigid body transformation calculated using custom MATLAB scripts as previously described, with MATLAB's default configurations for monomodal intensity-based registration and without initial transformation estimation. This automatic registration failed

for 6 out of 107 ROIs, which were then excluded from subsequent analyses. We calculated pixel-wise autocorrelation and cross-correlation as a function of distance as follows. Images were shifted by one voxel in each direction and padded using the intensity values of the pixels that were shifted out at that step. The pairwise linear correlation coefficient between pixel intensity values in DNA-PAINT and ExR staining channels, or PAINT-PAINT or ExR-ExR staining channels for autocorrelation, was calculated using MATLAB's 'corr' function. To calculate the half-maximal shift distance, we fit a third-degree polynomial (MATLAB's 'fit' with 'poly3') to the correlation or autocorrelation function, and used the best-fit curve to estimate the shift distance at which the correlation or autocorrelation reached 50% of its maximum value. Each of these calculations was repeated for each shift in the x- and y-dimensions. The mean differences in half-maximal shifts over x- and y-dimensions are plotted in Fig. 2h,i.

The total number of synaptic puncta for each image was calculated using custom MATLAB scripts (Extended Data Fig. 1j). Images were first passed through a 2D median filter of size (10, 10), binarized using Otsu's method and filtered to exclude puncta smaller than 150 nm in size. Synaptic puncta number was calculated from 2D connected components in the binary image with connectivity 26. Corresponding pairs of neighbouring synaptic puncta (within ~1 µm from one another) and single synaptic puncta were manually cropped from DNA-PAINT and ExR images and binarized as described above ($n = 50$ ROIs from 5 fields of view, 6 ROIs each, 1 culture batch). Puncta centroids were calculated from 2D connected components in the binary image (connectivity, 26) using MATLAB's 'regionprops' function. For cropped ROIs in which two synaptic puncta were counted after thresholding for both ExR and DNA-PAINT (Extended Data Fig. 1g–i; 27/50), the radial distance between puncta centroids (x_1, y_1) and (x_2, y_2) was calculated as $\mathrm{sqrt}((x_2 - x_1)^2 + (y_2 - y_1)^2)$. In Fig. 2j, the absolute value of the difference in distances between neighbouring synaptic puncta was normalized to the DNA-PAINT image. The coefficient of variation for distance between synaptic puncta imaged using ExR was calculated as the standard deviation of the difference in distance between pairs of synaptic puncta (PAINT − ExR) divided by the mean distance of the same pairs from DNA-PAINT.

Root mean squared error (RMS) between ExR and DNA-PAINT images was calculated as previously described. Briefly, a custom MATLAB script was used to implement a B-spline-based non-rigid registration between pre- and post-expansion images, yielding vector fields for deformation within the images. These vector fields were then used to calculate root-mean-square length distortions across varying lengths. For plotting, RMS error values were binned into measurement length increments of 1 µm and the mean RMS error within each bin is shown.

Decrowding analysis of manually segmented synapses. We compared the amplitude of signal intensity in the foreground (putative synapses) and background (everything else). First, we manually identified, on the basis of brightness and size of reference channel staining, 47–70 of the largest, brightest synapses per ~350 × 350 × 20 µm (physical units) field of view (see Supplementary Table 2 for exact numbers of synapses; one field of view per cortical layer, three cortical layers per sample, two mice per synaptic protein). We developed an automated method to segment putative synaptic puncta from background. First, background was subtracted from image stacks using ImageJ/Fiji's Rolling Ball algorithm with a radius of 50 pixels. Images were then binarized using a threshold calculated as seven times the standard deviation of the average intensity of manually identified background regions selected every tenth slice of the z-stack. Binary images were passed through a 3D median filter of radius 5 × 5 × 3 pixels to remove small puncta of non-specific staining. We then identified 3D connected components from the filtered binary stack using MATLAB's 'bwconncomp' function, with a pixel connectivity of 26, meaning that pixels are connected if their faces, edges or corners touch. Connected components smaller than 100 × 100 × 100 nm^3 (biological units) were removed, as most synapses are larger than this volume. ROIs, or putative synaptic puncta, were defined as 3D connected components of the filtered binary reference stack dilated using a disk structuring element with a radius of six pixels. A radius of six pixels (~100 nm, in biological units) was chosen because both pre- and post-synaptic proteins of the same synapse, but not other synapses, fall within this range (the synaptic cleft is ~12–20 nm[64]), which we confirmed by manual inspection. Segmented synapses with zero filtered connected components (synaptic puncta) in the reference channel were excluded from further analysis. We calculated the average intensity of background-subtracted images either within or outside of these dilated reference ROIs (Extended Data Fig. 2a) to measure signal increase within putative synapses relative to signal increase in the background. All images were acquired under the same microscope conditions to allow for comparison of mean signal intensity. The total volume of pre- or post-expansion staining test puncta located within dilated reference channel ROIs (Extended Data Fig. 2b) was calculated from binarized stacks of pre- and post-expansion channels (thresholded and filtered as described for the reference channel) after multiplying the dilated binary reference stack (for inside dilated reference ROIs) or its inverse (for just outside dilated reference ROIs, but still within the manually cropped synaptic area) by the binary pre- or post-expansion stack and calculating the sum of non-zero voxels for each product. Data are shown as the mean of each measure across the ~50 synapses per field of view, and the deviation was calculated as the standard error of these means across the nine fields of view (three fields of view for three animals) for each protein. We identified measured signal from one field of view from one animal as an outlier using the ROUT method[65] with $Q = 1\%$ in GraphPad Prism and excluded it from further analysis and visualization.

Quantification of synaptic properties. To compare volume and SNR of pre- and post-expansion staining (Extended Data Fig. 2c,d), we used the same dataset as for Extended Data Fig. 2a,b analysis. First, the background was subtracted from image stacks using ImageJ/Fiji's Rolling Ball algorithm with a radius of 50 pixels. Images were then binarized using a threshold calculated as seven times the standard deviation of the average intensity of manually identified background regions selected every tenth slice of the z-stack. We then identified and selected the biggest 3D connected components in pre- and post-staining test channels separately in each layer of somatosensory cortex (L1, L2/3 and L4), as these are most probably to be synapses. We calculated the voxel and signal intensity in the largest 3D connected components from 49–70 manually selected synapses (see Supplementary Table 2 for exact numbers for each layer, protein and mouse). The signal intensity was divided by the standard deviation of the background intensity to calculate the SNR.

Analysis of distortion introduced by ExR relative to pre-expansion staining. To calculate the number of synaptic puncta, background-subtracted images were first thresholded as described previously (on the basis of a multiple of the standard deviation of manually identified background regions) and passed through a 3 × 3 × 5 voxel (1 voxel = 17.16 × 17.16 × 40 nm^3) median filter. MATLAB's 'bwconncomp' function was used to find connected components (putative synaptic puncta, connectivity of 26) and connected components with fewer than 30 voxels of volume were excluded from further analysis. Distortion between pre- and post-expansion images was calculated as was done for distortion between DNA-PAINT and ExR images. Specifically, for the plots shown in Extended Data Fig. 3g–l, images were shifted by one voxel in each direction and padded using the intensity values of the pixels that were shifted out at that step. To calculate pixel-wise correlations and autocorrelations (Extended Data Fig. 3g–h), images were first normalized to their minimum and maximum intensity values. From these, we calculated the pairwise linear correlation coefficient (MATLAB's 'corr') between pixel intensity values in the pre- and post-expansion staining channels, and the pre-/post-expansion staining channels for autocorrelation. To calculate the half-maximal shift distance (Extended Data Fig. 2f,g), we fit a third-degree polynomial (MATLAB's 'fit' with 'poly3') to the correlation or autocorrelation as a function of shift distance and used the best-fit curve to estimate the shift distance at which the correlation or autocorrelation reached 50% of its maximum value. For the plots shown in Extended Data Fig. 3i,j, the correlation was calculated with a slight modification to account for differences in puncta volume. First, background-subtracted images were masked on the basis of the corresponding binary image. Second, non-zero pixels were divided by the mean intensity value in the non-zero regions. Finally, the correlation was calculated as the pairwise linear correlation coefficient (MATLAB's 'corr') between masked mean-normalized intensity values in the pre- and post-expansion staining channels. Mutually overlapped volume was calculated as the sum of non-zero pixels in the intersection of the binary pre- and post-expansion staining z-stacks, and normalized to the total puncta volume (sum of non-zero pixels in the binary z-stack) in the pre-expansion staining channel (Extended Data Fig. 3k,l). Each of these calculations was repeated for each shift in the x-, y- and z-directions. Synapses with zero puncta in the pre- or post-expansion staining channels were excluded from analysis.

Comparison between antigen retrieval and decrowding effect. Confocal images were obtained after immunostaining with antibodies against $Ca_v2.1$, PSD95 and Homer1 (Supplementary Fig. 2) and 6E10, 12F4 and SMI (Supplementary Fig. 6) with or without antigen retrieval treatment to compare signal quality for antigen retrieval vs ExR treatment. To determine whether antigen retrieval by heat denaturation alone is the dominant factor underlying increased signal quality afforded by ExR, we treated one group of tissues with a standard antigen-retrieval step (placing tissues in 20 mM sodium citrate at pH 8 and incubating at 100 °C for 30 s and 60 °C for 30 min)[11]. Tissues with or without this antigen-retrieval step were processed by ExR. Then, we compared the amplitude of signal intensity in foreground (putative synapses) and background (everything else). First, we manually identified, on the basis of brightness and size of reference channel staining (Homer1 for $Ca_v2.1$, Shank3 for PSD95 and Homer1), 30 of the largest and brightest synapses per ~350 × 350 × 20 µm (physical units) field of view ($n = 30$ synapses from 1 field of view from 1 mouse). We used the automated segmentation procedure and calculated mean signal intensity and volume as described above (see 'Decrowding analysis of manually segmented synapses').

Protein distance measurement and synaptic nanocolumn results analysis. For analysis, potential synapses were manually identified and selected on the basis of (1) the juxtaposition of pre-synaptic clusters and post-synaptic clusters and (2) the co-localization of clusters on the same side of the synapse (Figs. 2e and 4e–g,i–p). As camera pixel size was 167 nm (physical units) and the step size of the z-stack was 250 nm (physical units), the voxel size was not equivalent in all dimensions.

Because isometric voxels were necessary for subsequent analysis, each voxel was then subdivided into 12 smaller isometric voxels, each 83.3 nm (physical units) in all three dimensions. For comparisons of RIM1/2 and PSD95, one cluster was shifted in space to optimally overlap with the other cluster, as previously described[13,64]. The vector of this shift was determined by cross-correlation of the two clusters and defined both the trans-synaptic axis and the distance between the two clusters. For comparisons of RIM1/2 and $Ca_v2.1$, the shift distance was set as 0, and for comparisons of RIM1/2 and PSD95, putative synapses with a RIM1/2 to PSD95 peak-to-peak distance of less than 20 or greater than 180 nm (biological units) were rejected from further analysis, consistent with the dimensions of the active zone and PSD. Any synapses that extended beyond the z-range of the imaged stack were also excluded.

Autocorrelation ($g_a(r)$) and protein enrichment analyses were adapted from previously described localization data-based analyses[13,66]. The 3D autocorrelation function ($g_a(r)$) reports the increased probability of finding a similar signal at a distance (r) away from a given signal, and thus can be used to quantify the heterogeneity of the measured signal within a defined volume. The autocorrelation of each synaptic cluster was normalized by the autocorrelation of an object with the same shape and volume and that has a homogenous voxel intensity set to the average intensity of the synaptic cluster. Therefore, a synaptic cluster with a homogenous intensity will give a $g_a(r) = 1$ at all radii, and local intensity peaks within a synaptic cluster will result in a $g_a(r) > 1$ over a radius of the size of the region of high intensity. The cluster boundary was defined on the basis of fluorescent intensity after convolution with a spherical kernel ($r \approx 300$ nm).

The molecular distribution of two different protein clusters relative to one another was characterized using a cross-enrichment analysis. The cross-enrichment analysis was performed by measuring the angularly averaged voxel intensity of one protein cluster (measured cluster) as a function of the distance from the point of peak intensity in the other protein cluster (reference cluster, shifted in space as described above). This value was then normalized by the angularly averaged intensity (as a function of the distance from the point of peak intensity in the reference cluster) of an object of the same shape and volume as the measured cluster, with voxels set to the average intensity of the measured cluster. Regions of high local intensity in the measured cluster will result in values (normalized intensity) >1. The enrichment index was calculated by taking the average of the enrichment values within a radius of 60 nm from the peak of the reference cluster.

Synapse numbers (n) for the analysis from 2 mice:

Autocorrelations

$Ca_v2.1$ (Fig. 4e): $n = 144$ synapses (Layer 1), 101 synapses (Layer 23), 103 synapses (Layer 4)

PSD95 (Fig. 4f): $n = 144$ synapses (Layer 1), 101 synapses (Layer 23), 103 synapses (Layer 4)

RIM1/2 (Fig. 4g): $n = 144$ synapses (Layer 1), 101 synapses (Layer 23), 103 synapses (Layer 4)

Enrichment analysis

RIM1/2 enrichment to PSD95 peak (Fig. 4i,j): $n = 153$ synapses (Layer 1), 103 synapses (Layer 23), 108 synapses (Layer 4)

PSD95 enrichment to RIM1/2 peak (Fig. 4k,l): $n = 152$ synapses (Layer 1), 102 synapses (Layer 23), 108 synapses (Layer 4)

$Ca_v2.1$ enrichment to RIM1/2 peak (Fig. 4m,n): $n = 150$ synapses (Layer 1), 103 synapses (Layer 23), 107 synapses (Layer 4)

RIM1/2 enrichment to $Ca_v2.1$ peak (Fig. 4o,p): $n = 153$ synapses (Layer 1), 99 synapses (Layer 23), 108 synapses (Layer 4)

Enrichment index values (mean ± s.d.):

RIM1/2 to PSD95 peak (Fig. 4j): 1.585 ± 0.330 (Layer 1), 1.535 ± 0.358 (Layer 23), 1.545 ± 0.332 (Layer 4)

PSD95 to RIM1/2 peak (Fig. 4l): 1.611 ± 0.308 (Layer 1), 1.632 ± 0.269 (Layer 23), 1.622 ± 0.285 (Layer 4)

$Ca_v2.1$ to RIM1/2 peak (Fig. 4n): 1.510 ± 0.364 (Layer 1), 1.359 ± 0.330 (Layer 23), 1.452 ± 0.314 (Layer 4)

RIM1/2 to $Ca_v2.1$ peak (Fig. 4p): 1.493 ± 0.330 (Layer 1), 1.317 ± 0.311 (Layer 23), 1.422 ± 0.322 (Layer 4)

Analysis of the Alzheimer's results. Comparison of Aβ42 volume in WT vs 5xFAD. For Supplementary Fig. 5b, 3D image stacks of Aβ42 and SMI312 staining were background subtracted via rolling-ball background subtraction with a 200 pixel radius using ImageJ/Fiji. For each colour channel, the standard deviation for the background was calculated using a 75 × 75 pixel window. Subsequently, each colour channel was binarized by applying a threshold of 28 times the standard deviation of the background. This value was determined by evaluating the amount of thresholding required to remove putative non-specific staining spots. Finally, after binarization, the volume of Aβ42 and SMI312 for each field of view was determined by adding up the segmented pixels of each colour channel.

Distance measurement between clusters. To calculate the distance between adjacent clusters for either Aβ42 or $K_v7.2$ (Fig. 6d), clusters that line along SMI312 neurofilaments were manually cropped out in 3D. Then, after applying rolling-ball background subtraction with a 100 pixel radius, the centroid of each cluster was annotated manually using ImageJ/Fiji in 3D. Given that the spacing between clusters is much larger than the size of each cluster, we reasoned that manual labelling of the centroids incurs minimal error. Finally, the distance between adjacent clusters was calculated in 3D.

Calculation of Aβ42 and $K_v7.2$ cluster diameter. After applying rolling-ball background subtraction with a 100 pixel radius to 3D fields of view of Aβ42 and $K_v7.2$ staining, overlapping $K_v7.2$ and Aβ42 clusters were manually cropped out. After calculating the standard deviation of the background of each channel, the cropped images were binarized by applying a threshold ten times the standard deviation of the background. The volume of each cluster was then identified via connected component analysis using MATLAB's 'bwconncomp' function. Finally, the centroid and principal axis length of each cluster were determined using the associated 'regionprops' function, which models each connected component region as an ellipsoid. The centroid values were then used to calculate the distance between overlapped Aβ42 and $K_v7.2$ clusters (Fig. 6g–i).

Aβ42 and Kv7.2 cluster shape analysis. ROIs containing single Aβ42 puncta that were part of a periodic chain-like structure were manually identified ($n = 55$ ROIs, 5 ROIs per field of view, from 11 fields of view from 2 mice) from background-subtracted images (ImageJ/Fiji's Rolling Ball algorithm, radius of 50 pixels). To visualize the 3D shape of Aβ42 and $K_v7.2$ puncta within these ROIs, we resliced the image stack along both transverse dimensions at equal spacing to the axial dimension. We display the middle slice in each stack in the x-y plane in Fig. 7a(ii)–d(ii) and the middle slice in each stack in the x-y, y-z and x-z planes in Supplementary Fig. 8a (where x- and y-directions are transverse, and z-direction is axial). To quantify shape features, we used CellProfiler's[67] Watershed[68] segmentation module to segment puncta within manually extracted ROIs using a footprint of 30 pixels for each channel. A custom MATLAB script was deployed to calculate the number of puncta in each channel, mean and maximum volume and surface area of these puncta, length of the three principal axes of the ellipsoid that have the same normalized second central moments as the region for the largest puncta, and the total volume of puncta overlap between Aβ42 and $K_v7.2$ as the number of non-zero pixels in the intersection of the binary image stacks. To quantify the statistical significance of the relationships between these measures, either two-tailed paired t-tests or simple linear regression were used as described in the text.

Expansion factor and measurement of the root mean square error. A Thy1-YFP mouse was perfused as described above and 50 µm coronal sections were prepared using a vibratome. Before expansion, yellow fluorescent protein (YFP) fluorescence was imaged in six fields of view from the cortex of three cortical slices. Subsequently, these slices were processed with the ExR protocol as described above. Expanded slices were then labelled with a primary antibody against green fluorescent protein (GFP; ThermoFisher, A-11122) and a secondary antibody (see Supplementary Table 10 for list of antibodies). The same fields of view imaged pre-expansion were identified and confocal images of the antibody staining were acquired. Pre- and post-ExR images were acquired on an Andor spinning disk (CSU-X1 Yokogawa) confocal microscope with a 40 × 1.15 numerical aperture water objective.

To determine distortion arising from the process of ExR, pre- and post-expansion images were aligned and deformations in images were determined as described previously. Briefly, pre- and post-ExR images were background subtracted with a Rolling Ball background-subtraction algorithm (ImageJ/Fiji) with a 200 pixel radius. Then, corresponding confocal planes from pre and post images were identified and registered using Fiji's Turboreg method, allowing for scaling and rigid rotation. Then, a custom MATLAB script was used to implement a B-spline-based non-rigid registration between pre- and post-expansion images, yielding vector fields for deformation within the images. These vector fields were then used to calculate root-mean-square length distortions across varying lengths.

To calculate the expansion factor, the physical distances between feature-containing YFP structures (for example, dendrites and axons) in fluorescent protein-containing specimens were measured in pre- and post-ExR images. In cases of 5xFAD or C57BL/6 mice, DAPI staining of neighbouring cells was used to measure corresponding distances in pre- and post-ExR images, and the expansion factor was calculated by dividing the distances.

Tables listing the chemicals and antibodies used are available as Supplementary Information.

ExR protocol.

1. Mouse tissue slices
   i. Anaesthetize mice using isoflurane in oxygen and perfuse with 10 ml 2% acrylamide in PBS followed by 10 ml 30% acrylamide and 4% paraformaldehyde in PBS.
   ii. Collect brains and incubate in 20 ml of the same fixative solution (30% acrylamide and 4% formaldehyde in PBS) at 4 °C overnight.
   iii. Transfer fixed brains to 100 mM glycine at 4 °C for 6 h.
   iv. Store tissues in PBS at 4 °C for long-term storage.
   v. Slice tissues on a vibrating microtome to a thickness of 50–100 µm.

2. Gelation

A. Gelling for first expansion

i. Incubate brain slices in the first gelling solution for 30 min at 4 °C.
ii. Place brain slices with excess first gelling solution between two no. 1.5 coverglasses separated by two pieces of no. 1.5 coverglasses, and then incubate at 37 °C for 2 h.
iii. Cut out gels from the chamber and incubate with denaturation buffer (200 mM SDS, 200 mM NaCl and 50 mM Tris pH 9) for 1 h at 95 °C.
iv. Wash gels four times with DI water in shaker and expand gels in DI water at 4 °C overnight.

B. Re-embedding

i. Incubate expanded first gels in re-embedding solution twice for 1 h each time in shaker at room temperature.
ii. Transfer gels between no. 1.5 coverglasses separated by slide glass and incubate with excess re-embedding solution at 45 °C for 2 h.
iii. Wash gels three times with PBS in shaker.

C. Third gelling

i. Incubate the re-embedded gels in the third gelling solution twice for 1 h each time in shaker at room temperature.
ii. Transfer gels between no. 1.5 coverglasses separated by slide glass and incubate at 60 °C for 1 h.
iii. Wash gels four times with DI water in shaker and expand gels in DI water at 4 °C overnight.
iv. Trim gels axially to 1 mm thickness.

3. Staining

i. Incubate gels in blocking solution (0.5% Triton X-100, 5% NDS in PBS) for 2 h at room temperature.
ii. Incubate gels with primary antibodies in '0.25T' blocking buffer (0.25% Triton X-100, 5% NDS in PBS) overnight at 4 °C.
iii. Wash gels with washing buffer (0.1% Triton X-100 in PBS) six times for 1 h each time.
iv. Incubate gels with secondary antibodies in blocking solution at 4 °C overnight.
v. Wash gels with washing buffer (0.1% Triton X-100 in PBS) six times for 1 h each time and expand gels in DI water for 20X expansion or 0.05x PBS for 15X expansion.

Reporting summary. Further information on research design is available in the Nature Research Reporting Summary linked to this article.

Data availability

The main data supporting the results in this study are available within the paper and its Supplementary Information. The raw and analysed datasets generated during the study are too large to be publicly shared, yet they are available for research purposes from the corresponding authors on reasonable request. Source data are provided with this paper.

Code availability

The custom code used in this study is available on Zenodo at https://doi.org/10.5281/zenodo.6383293 and on GitHub at https://github.com/schroeme/ExR.

Received: 22 November 2020; Accepted: 22 June 2022;
Published online: 29 August 2022

References

1. Sydor, A. M., Czymmek, K. J., Puchner, E. M. & Mennella, V. Super-resolution microscopy: from single molecules to supramolecular assemblies. *Trends Cell Biol.* **25**, 730–748 (2015).
2. Wassie, A. T., Zhao, Y. & Boyden, E. S. Expansion microscopy: principles and uses in biological research. *Nat. Methods* **16**, 33–41 (2019).
3. Chen, F., Tillberg, P. W. & Boyden, E. S. Expansion microscopy. *Science* **347**, 543–548 (2015).
4. Chang, J. B. et al. Iterative expansion microscopy. *Nat. Methods* **14**, 593–599 (2017).
5. Chen, F. et al. Nanoscale imaging of RNA with expansion microscopy. *Nat. Methods* **13**, 679–684 (2016).
6. Tillberg, P. W. et al. Protein-retention expansion microscopy of cells and tissues labeled using standard fluorescent proteins and antibodies. *Nat. Biotechnol.* **34**, 987–992 (2016).
7. Zhao, Y. et al. Nanoscale imaging of clinical specimens using pathology-optimized expansion microscopy. *Nat.* Biotechnol. **35**, 757–764 (2017).
8. Dani, A., Huang, B., Bergan, J., Dulac, C. & Zhuang, X. Superresolution imaging of chemical synapses in the brain. *Neuron* **68**, 843–856 (2010).
9. Monteiro, P. & Feng, G. SHANK proteins: roles at the synapse and in autism spectrum disorder. *Nat. Rev. Neurosci.* **18**, 147–157 (2017).
10. Dolphin, A. C. & Lee, A. Presynaptic calcium channels: specialized control of synaptic neurotransmitter release. *Nat. Rev. Neurosci.* **21**, 213–229 (2020).
11. Xiao, B., Cheng, Tu,J. & Worley, P. F. Homer: a link between neural activity and glutamate receptor function. *Curr. Opin. Neurobiol.* **10**, 370–374 (2000).
12. Szumlinski, K. K., Kalivas, P. W. & Worley, P. F. Homer proteins: implications for neuropsychiatric disorders. *Curr. Opin. Neurobiol.* **16**, 251–257 (2006).
13. Zhu, F. et al. Architecture of the mouse brain synaptome. *Neuron* **99**, 781–799.e10 (2018).
14. Vazquez, L. E., Chen, H. J., Sokolova, I., Knuesel, I. & Kennedy, M. B. SynGAP regulates spine formation. *J. Neurosci.* **24**, 8862–8872 (2004).
15. Davydova, D. et al. Bassoon specifically controls presynaptic P/Q-type Ca2+ channels via RIM-binding protein. *Neuron* **82**, 181–194 (2014).
16. Peça, J. et al. Shank3 mutant mice display autistic-like behaviours and striatal dysfunction. *Nature* **472**, 437–442 (2011).
17. Graf, E. R. et al. RIM promotes calcium channel accumulation at active zones of the *Drosophila* neuromuscular junction. *J. Neurosci.* **32**, 16586–16596 (2012).
18. Kiyonaka, S. et al. RIM1 confers sustained activity and neurotransmitter vesicle anchoring to presynaptic Ca2+ channels. *Nat. Neurosci.* **10**, 691–701 (2007).
19. Frank, T. et al. Bassoon and the synaptic ribbon organize Ca2+ channels and vesicles to add release sites and promote refilling. *Neuron* **68**, 724–738 (2010).
20. El-Husseini, A. E., Schnell, E., Chetkovich, D. M., Nicoll, R. A. & Bredt, D. S. PSD-95 involvement in maturation of excitatory synapses. *Science* **290**, 1364–1368 (2000).
21. Migaud, M. et al. Enhanced long-term potentiation and impaired learning in mice with mutant postsynaptic density-95 protein. *Nature* **396**, 433–439 (1998).
22. Hayashi, M. K. et al. The postsynaptic density proteins Homer and Shank form a polymeric network structure. *Cell* **137**, 159–171 (2009).
23. Tang, A. H. et al. A trans-synaptic nanocolumn aligns neurotransmitter release to receptors. *Nature* **536**, 210–214 (2016).
24. Heine, M. & Holcman, D. Asymmetry between pre- and postsynaptic transient nanodomains shapes neuronal communication. *Trends Neurosci.* **43**, 182–196 (2020).
25. Hruska, M., Henderson, N., Le Marchand, S. J., Jafri, H. & Dalva, M. B. Synaptic nanomodules underlie the organization and plasticity of spine synapses. *Nat. Neurosci.* **21**, 671–682 (2018).
26. Rebola, N. et al. Distinct nanoscale calcium channel and synaptic vesicle topographies contribute to the diversity of synaptic function. *Neuron* **104**, 693–710.e9 (2019).
27. Brockmann, M. M. et al. RIM-BP2 primes synaptic vesicles via recruitment of Munc13-1 at hippocampal mossy fiber synapses. *eLife* **8**, e43243 (2019).
28. Holderith, N. et al. Release probability of hippocampal glutamatergic terminals scales with the size of the active zone. *Nat. Neurosci.* **15**, 988–997 (2012).
29. Eggermann, E., Bucurenciu, I., Goswami, S. P. & Jonas, P. Nanodomain coupling between Ca2+ channels and sensors of exocytosis at fast mammalian synapses. *Nat. Rev. Neurosci.* **13**, 7–21 (2012).
30. Canter, R. G., Penney, J. & Tsai, L. H. The road to restoring neural circuits for the treatment of Alzheimer's disease. *Nature* **539**, 187–196 (2016).
31. Oakley, H. et al. Intraneuronal β-amyloid aggregates, neurodegeneration, and neuron loss in transgenic mice with five familial Alzheimer's disease mutations: potential factors in amyloid plaque formation. *J. Neurosci.* **26**, 10129–10140 (2006).
32. Chao, L. L. et al. Associations between white matter hyperintensities and β amyloid on integrity of projection, association, and limbic fiber tracts measured with diffusion tensor MRI. *PLoS ONE* **8**, e65175 (2013).
33. Song, S. K., Kim, J. H., Lin, S. J., Brendza, R. P. & Holtzman, D. M. Diffusion tensor imaging detects age-dependent white matter changes in a transgenic mouse model with amyloid deposition. *Neurobiol. Dis.* **15**, 640–647 (2004).
34. Dong, J. W. et al. Diffusion MRI biomarkers of white matter microstructure vary nonmonotonically with increasing cerebral amyloid deposition. *Neurobiol. Aging* **89**, 118–128 (2020).
35. Gail Canter, R. et al. 3D mapping reveals network-specific amyloid progression and subcortical susceptibility in mice. *Commun. Biol.* **2**, 1–12 (2019).
36. Dunn, A. R. & Kaczorowski, C. C. Regulation of intrinsic excitability: roles for learning and memory, aging and Alzheimer's disease, and genetic diversity. *Neurobiol. Learn. Mem.* **164**, 107069 (2019).
37. Chong, S. Y. C. et al. Neurite outgrowth inhibitor Nogo-A establishes spatial segregation and extent of oligodendrocyte myelination. *Proc. Natl Acad. Sci. USA* **109**, 1299–1304 (2012).
38. Brohawn, S. G. et al. The mechanosensitive ion channel traak is localized to the mammalian node of Ranvier. *eLife* **8**, 1–22 (2019).

39. Dupree, J. L. et al. Oligodendrocytes assist in the maintenance of sodium channel clusters independent of the myelin sheath. *Neuron Glia Biol.* **1**, 179–192 (2004).
40. Lubetzki, C., Sol-Foulon, N. & Desmazières, A. Nodes of Ranvier during development and repair in the CNS. *Nat. Rev. Neurol.* **16**, 426–439 (2020).
41. Shah, N. H. & Aizenman, E. Voltage-gated potassium channels at the crossroads of neuronal function, ischemic tolerance, and neurodegeneration. *Transl. Stroke Res.* **5**, 38–58 (2014).
42. Hessler, S. et al. β-secretase BACE1 regulates hippocampal and reconstituted M-currents in a β-subunit-like fashion. *J. Neurosci.* **35**, 3298–3311 (2015).
43. Ciccone, R. et al. Amyloid β-induced upregulation of Nav1.6 underlies neuronal hyperactivity in Tg2576 Alzheimer's disease mouse model. *Sci. Rep.* **9**, 1–18 (2019).
44. Ghatak, S. et al. Mechanisms of hyperexcitability in Alzheimer's disease hiPSC-derived neurons and cerebral organoids vs. isogenic control. *eLife* **8**, e50333 (2019).
45. Lim, C. J., Lee, S. Y., Teramoto, J., Ishihama, A. & Yan, J. The nucleoid-associated protein Dan organizes chromosomal DNA through rigid nucleoprotein filament formation in *E. coli* during anoxia. *Nucleic Acids Res.* **41**, 746–753 (2013).
46. Xu, K., Zhong, G. & Zhuang, X. Actin, spectrin, and associated proteins form a periodic cytoskeletal structure in axons. *Science* **339**, 452–456 (2013).
47. Winardhi, R. S., Castang, S., Dove, S. L. & Yan, J. Single-molecule study on histone-like nucleoid-structuring protein (H-NS) paralogue in *Pseudomonas aeruginosa*: MvaU bears DNA organization mode similarities to MvaT. *PLoS ONE* **9**, e112246 (2014).
48. Leterrier, C. et al. Nanoscale architecture of the axon initial segment reveals an organized and robust scaffold. *Cell Rep.* **13**, 2781–2793 (2015).
49. Chiang, Y. L. et al. Atomic force microscopy characterization of protein fibrils formed by the amyloidogenic region of the bacterial protein MinE on mica and a supported lipid bilayer. *PLoS ONE* **10**, e0142506 (2015).
50. Prakash, K. et al. Superresolution imaging reveals structurally distinct periodic patterns of chromatin along pachytene chromosomes. *Proc. Natl Acad. Sci. USA* **112**, 14635–14640 (2015).
51. Makky, A., Bousset, L., Polesel-Maris, J. & Melki, R. Nanomechanical properties of distinct fibrillar polymorphs of the protein α-synuclein. *Sci. Rep.* **6**, 37970 (2016).
52. D'Este, E., Kamin, D., Göttfert, F., El-Hady, A. & Hell, S. W. STED nanoscopy reveals the ubiquity of subcortical cytoskeleton periodicity in living neurons. *Cell Rep.* **10**, 1246–1251 (2015).
53. D'Este, E. et al. Subcortical cytoskeleton periodicity throughout the nervous system. *Sci. Rep.* **6**, (2016).
54. Qu, Y., Hahn, I., Webb, S. E. D., Pearce, S. P. & Prokop, A. Periodic actin structures in neuronal axons are required to maintain microtubules. *Mol. Biol. Cell* **28**, 296–308 (2017).
55. Bose, K., Lech, C. J., Heddi, B. & Phan, A. T. High-resolution AFM structure of DNA G-wires in aqueous solution. *Nat. Commun.* **9**, 1959 (2018).
56. Ku, T. et al. Multiplexed and scalable super-resolution imaging of three-dimensional protein localization in size-adjustable tissues. *Nat. Biotechnol.* **34**, 973–981 (2016).
57. M'Saad, O. & Bewersdorf, J. Light microscopy of proteins in their ultrastructural context. *Nat. Commun.* https://doi.org/10.1038/s41467-020-17523-8 (2020).
58. Gambarotto, D. et al. Imaging cellular ultrastructures using expansion microscopy (U-ExM). *Nat. Methods* **16**, 71–74 (2019).
59. Zwettler, F. U. et al. Molecular resolution imaging by post-labeling expansion single-molecule localization microscopy (Ex-SMLM). *Nat. Commun.* **11**, 1–11 (2020).
60. Chen, F. et al. Nanoscale imaging of RNA with expansion microscopy. *Nat. Methods* **13**, 679–684 (2016).
61. Klapoetke, N. C. et al. Independent optical excitation of distinct neural populations. *Nat. Methods* **11**, 338–346 (2014).
62. Saka, S. K. et al. Immuno-SABER enables highly multiplexed and amplified protein imaging in tissues. *Nat. Biotechnol.* **37**, 1080–1090 (2019).
63. Schnitzbauer, J. et al. Super-resolution microscopy with DNA-PAINT. *Nat. Protoc.* **12**, 1198–1228 (2017).
64. Savtchenko, L. P. & Rusakov, D. A. The optimal height of the synaptic cleft. *Proc. Natl Acad. Sci. USA* **104**, 1823–1828 (2007).
65. Motulsky, H. J. & Brown, R. E. Detecting outliers when fitting data with nonlinear regression - a new method based on robust nonlinear regression and the false discovery rate. *BMC Bioinformatics* **7**, 123 (2006).
66. Chen, J. H., Blanpied, T. A. & Tang, A. H. Quantification of trans-synaptic protein alignment: a data analysis case for single-molecule localization microscopy. *Methods* **174**, 72–80 (2020).
67. McQuin, C. et al. CellProfiler 3.0: next-generation image processing for biology. *PLoS Biol.* **16**, e2005970 (2018).
68. Mangan, A. P. & Whitaker, R. T. Partitioning 3D surface meshes using watershed segmentation. *IEEE Trans. Vis. Comput. Graph.* **5**, 308–321 (1999).

Acknowledgements

We thank T. Biederer, C. Zhang and Y. Liu for antibody advice, S. Alon and K. Piatkevich for trainings and discussions; B. Kang for decrowding analysis advice; and D. Goodwin for instructions and scripts for manual image registration. D.S. acknowledges funding from NIH K99/R00 Pathway to independence Award (K99GM126277 and R00GM126277); M.E.S was supported by the National Science Foundation Graduate Research Fellowship under Grant No. 1745302 and the MathWorks Science Fellowship; A.-H.T. acknowledges funding from NARSAD; E.D.N. acknowledges funding from Alana Down Syndrome Center and Robert A. and Renee E. Belfer Foundation; P.Y. acknowledges funding from NIH RF1 MH124606 and NIH Director's Pioneer Award DP1 GM133052; L.-H.T. acknowledges funding from Robert A and Renee E Belfer Family Foundation, Alana Down Syndrome Center, Ludwig Family Foundation, the JPB Foundation, NIH Grants RO1 NS102730 and RF1 AG054321; T.A.B acknowledges funding from NIMH R37MH080046 and R01MH119826; E.S.B. acknowledges funding from the Ludwig Family Foundation, the Open Philanthropy Project, John Doerr, Lisa Yang and the Tan-Yang Center for Autism Research at MIT, the US Army Research Laboratory and the US Army Research Office under contract/grant number W911NF1510548; Charles Hieken, Tom Stocky, Kathleen Octavio, Lore McGovern, Good Ventures; NIH Director's Pioneer Award 1DP1NS087724, NIH R01MH110932, NIH R01EB024261, NIH U24NS109113, NIH R37MH08004613, NIH 1RM1HG008525, NIH 1R01AG070831, NIH 1R56AG069192 and NIH R01MH124606; funding from the European Research Council (ERC) under the European Union's Horizon 2020 research and innovation programme (grant agreement No 835102); and HHMI. We also thank B. Chow and E. Betzig, as well as many current and past members of the Synthetic Neurobiology group, for discussions. The funders had no role in the study design, data collection and analysis, decision to publish or preparation of the manuscript.

Author contributions

D.S. initiated work, developed the ExR technology, contributed key ideas, designed and performed experiments and interpreted data for all projects, and wrote and edited the manuscript. J.K. contributed key ideas, designed and performed experiments for all projects, performed analysis for decrowding, and wrote and edited the manuscript. A.T.W. co-developed approaches to measuring decrowding, contributed key ideas to ExR technology development and decrowding analysis, designed and performed experiments, analysed data for all projects, and wrote and edited the manuscript. M.E.S contributed key ideas, designed and implemented analysis, visualization and statistical tests for all projects, created the schematic in Fig. 1 with input from others, and wrote and edited the manuscript. Z.P. contributed key ideas, designed and performed experiments, and conducted analysis for the Alzheimer's project. T.B.T. contributed key ideas, designed experiments, created software, analysed and interpreted data related to synapses, and helped in writing and editing the manuscript. A.-H.T. created software and analysed data related to synapses. E.D.N. designed experiments, interpreted experimental data for the Alzheimer's project, and helped in writing and editing the manuscript. J.Z.Y. oversaw the Alzheimer's project and designed experiments for it. H.S. performed DNA-PAINT validation experiments. D.P. prepared cultured neurons. P.Y. contributed key ideas and designed experiments for DNA-PAINT validation. L.-H.T. conceptualized and initiated the Alzheimer's project, provided oversight and funding, contributed key ideas and designed experiments, and helped in writing and editing the manuscript. T.A.B. contributed key ideas, designed experiments and interpreted data for the synapse project, and helped in writing and editing the manuscript. E.S.B. supervised the project, initiated work, contributed key ideas, designed experiments, helped with data analysis and interpretation, and wrote and edited the manuscript.

Competing interests

D.S., A.T.W., J.K. and E.S.B. are co-inventors on a patent application for ExR (US 2020/0271556 A1). E.S.B. is co-founder of a company seeking to deploy applications of ExM-related technologies. The other authors declare no competing interests.

Additional information

Extended data is available for this paper at https://doi.org/10.1038/s41551-022-00912-3.

Supplementary information The online version contains supplementary material available at https://doi.org/10.1038/s41551-022-00912-3.

Correspondence and requests for materials should be addressed to Li-Huei Tsai, Thomas A. Blanpied or Edward S. Boyden.

Peer review information *Nature Biomedical Engineering* thanks Laurent Nguyen, Markus Sauer and the other, anonymous, reviewer(s) for their contribution to the peer review of this work.

Reprints and permissions information is available at www.nature.com/reprints.

Publisher's note Springer Nature remains neutral with regard to jurisdictional claims in published maps and institutional affiliations.

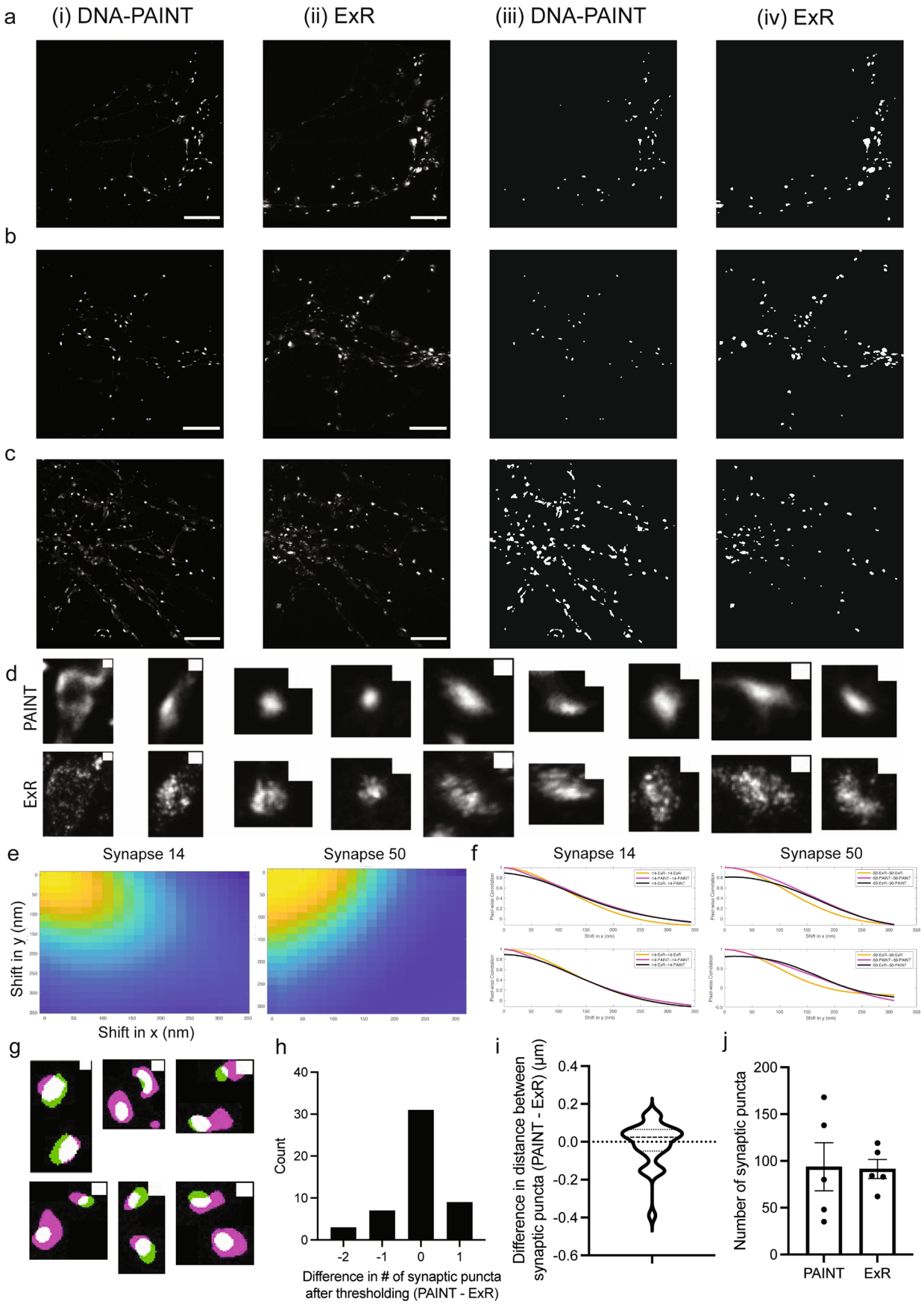

Extended Data Fig. 1 | See next page for caption.

Extended Data Fig. 1 | Comparison of synaptic nanostructures imaged using DNA-PAINT and ExR in cultured neurons. (a-c) Three representative fields of view imaged using DNA-PAINT (i) and ExR (ii) after rigid body registration to DNA-PAINT images. Scale bar = 5 μm. (iii-iv) Processed, binary versions of (i) and (ii) used to automatically count synaptic puncta number and pairwise distances. Scale bar, 5μm. **(d)** Representative manually-cropped matched synaptic ROIs for DNA-PAINT (top row) and ExR (bottom row), used for the distortion analysis shown in Fig. 2h,i (scale bar = 250 nm). **(e)** Pixel-wise correlation between min-max normalized ExR and DNA-PAINT channels as a function of shift distance in x- and y-directions for two randomly selected synaptic ROIs. **(f)** Pixel-wise autocorrelation between min-max normalized DNA-PAINT (PAINT-PAINT, magenta), ExR (ExR-ExR, yellow), and pixel-wise correlation between DNA-PAINT and ExR (PAINT-ExR, black) as a function of shift distance in x- and y-directions for the synaptic ROIs shown in **(e)**. **(g)** Representative manually-cropped pairs of synaptic puncta used to generate the data shown in Fig. 2j and panel i. Shown is an overlay of DNA-PAINT (green) and ExR (magenta) binary masks (scale bar = 250 nm). **(h)** Histogram of difference in number of synaptic puncta counted after thresholding pairs of synaptic puncta. **(i)** Difference in radial distance between pairs of synaptic puncta, DNA-PAINT – ExR (mean = -0.008854, 95% CI [-0.05419, 0.03649]). **(j)** Total number of synaptic puncta for the five fields of view imaged using DNA-PAINT and ExR (two-sided paired t-test, $p = 0.9271$, $t = 0.09735$, $df = 4$). All data are from 5 ROIs from 3 wells of one cultured neuron batch. Shown are images from one representative experiment from two independent replicates.

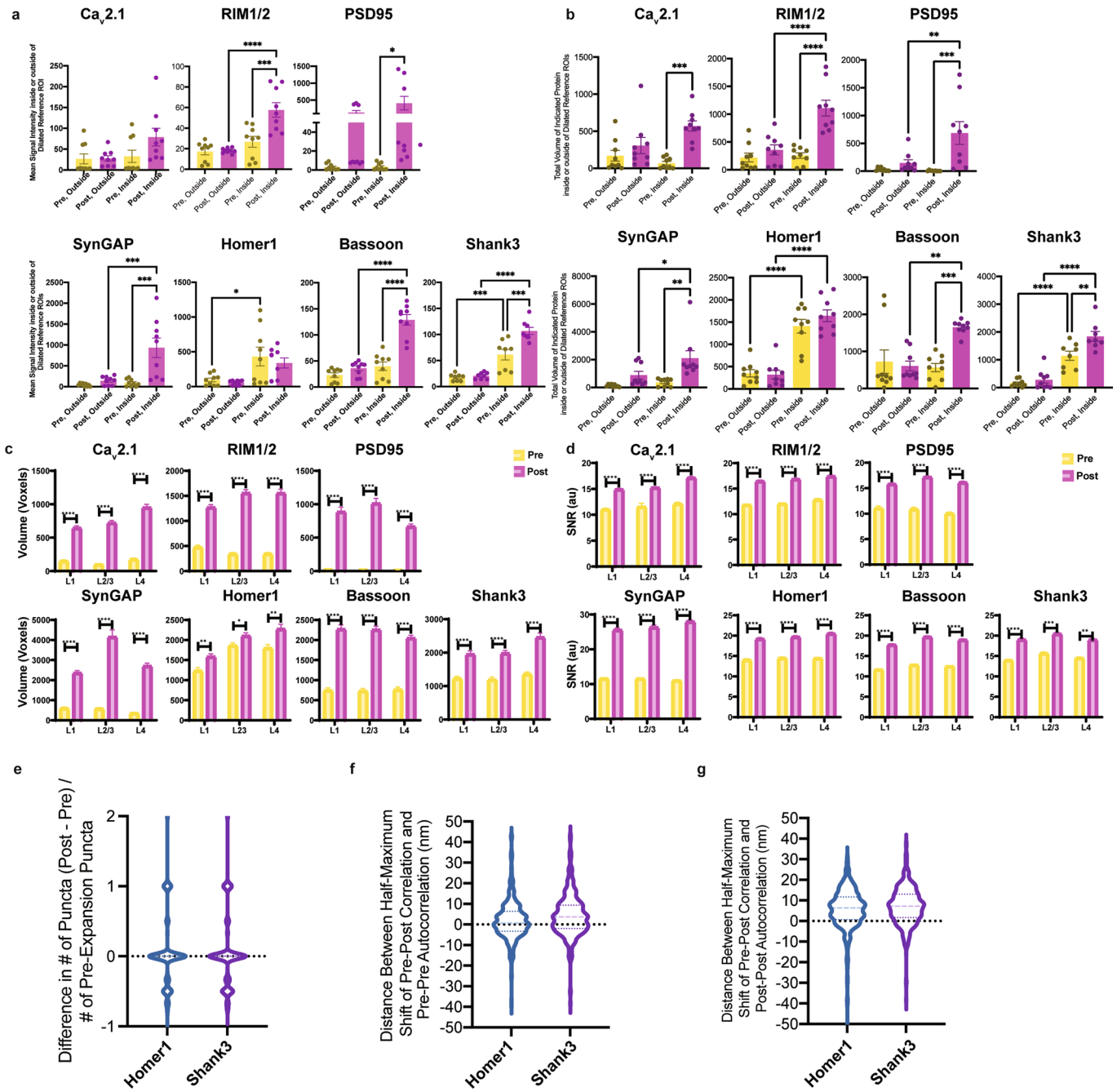

Extended Data Fig. 2 | See next page for caption.

Extended Data Fig. 2 | Analysis of the ExR decrowding effect. (a, b) Quantification of decrowding in a set of manually identified synapses. Statistical significance was determined using Sidak's multiple comparisons test on two-sided t-tests following ANOVA (*$P \leq 0.05$, **$P \leq 0.01$, ***$P < 0.001$, ****$P < 0.0001$, here and throughout the paper, and plotted is the mean, with error bars representing standard error of the mean (SEM), here and throughout the paper). **(a)** Mean signal intensity inside and outside of (that is, nearby to) dilated reference ROIs for pre- and post-expansion stained manually-identified synapses (Supplementary Table 2 for numbers of technical and biological replicates)). Data points represent the mean across all synapses from a single field of view. **(b)** Total volume (in voxels; 1 voxel = 17.16 × 17.15 × 40, or 11,779, nm^3) of signals inside and outside of dilated reference ROIs, in both cases within cropped images containing one visually identified synapse (Supplementary Fig. 3h), for pre- and post-expansion stained manually-identified synapses (Supplementary Table 2 for numbers of biological and technical replicates). Data points represent the mean across all synapses for 3 fields of view from 3 biological replicates (n = 9 fields of view total per protein). **(c)** Mean voxel size and **(d)** mean signal-to-noise (SNR) ratio of pre- and post-expansion immunostaining showing 7 proteins in somatosensory cortex regions L1, L2/3, and L4 of 3 mice. Plotted is mean and SEM. To compare the 3D voxel size and SNR of pre- and post-expansion stained synapses for each of the seven proteins, three two-sided t-tests (one for each layer) were run (n = 49–70 puncta per layer from 3 mice; Supplementary Table 2 for exact n values). Statistical significance was determined using multiple t-tests corrected using the Holm-Sidak method, with alpha = 0.05. **(e)** Population distribution (violin plot of density, with a dashed line at the median and dotted lines at the quartiles) of the fractional difference in the number of synaptic puncta between post- and pre-expansion staining channels for Homer1 and Shank3 (n = 480 synapses from 3 mice). **(f)** Population distribution of the difference in distance (in nm) between the shift at which the correlation is half maximal half-maximal shift for pre-pre autocorrelation and post-pre correlation (calculated pixel-wise between intensity values normalized to the minimum and maximum of the image, see Methods) for x-, y-, and z-directions (x- and y-directions being transverse, z-direction being axial) for Homer1 and Shank3 (n = 458 synapses, 3 directions each, from 3 mice). **(g)** Same as **(f)**, for post-post autocorrelation and pre-post correlation.

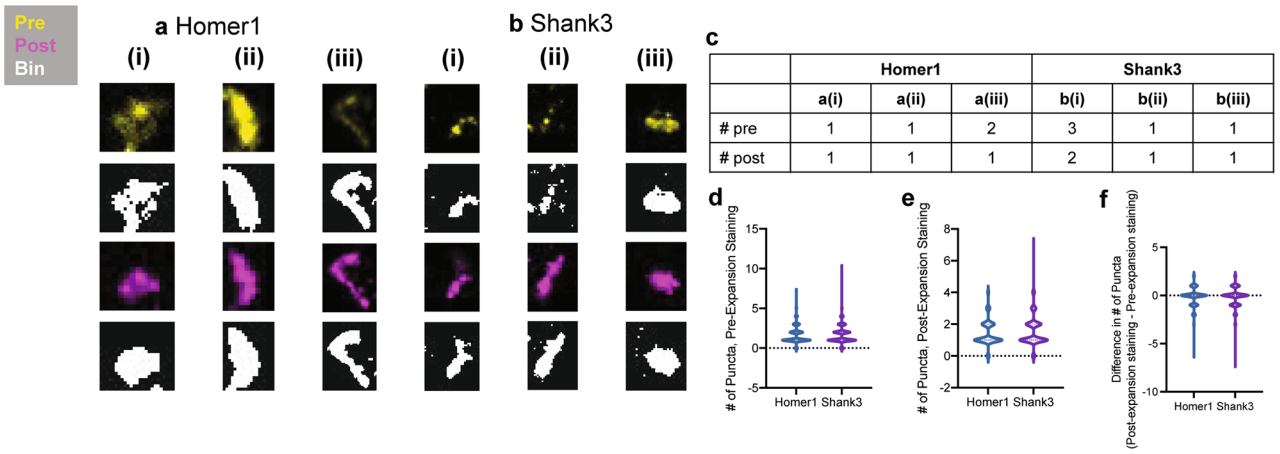

c

	Homer1			Shank3		
	a(i)	a(ii)	a(iii)	b(i)	b(ii)	b(iii)
# pre	1	1	2	3	1	1
# post	1	1	1	2	1	1

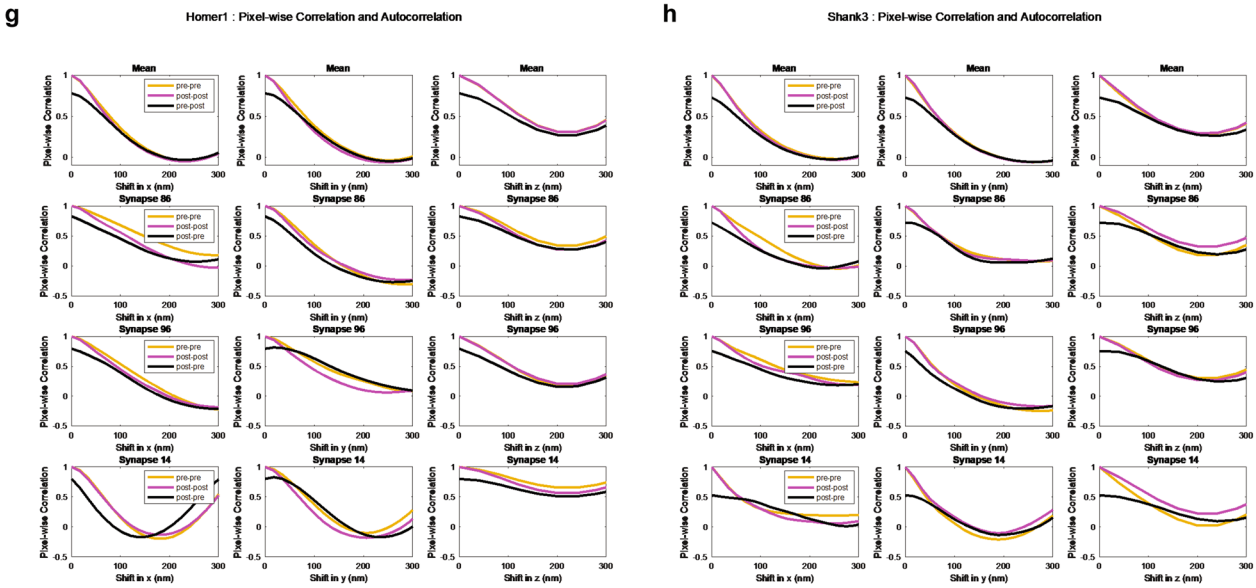

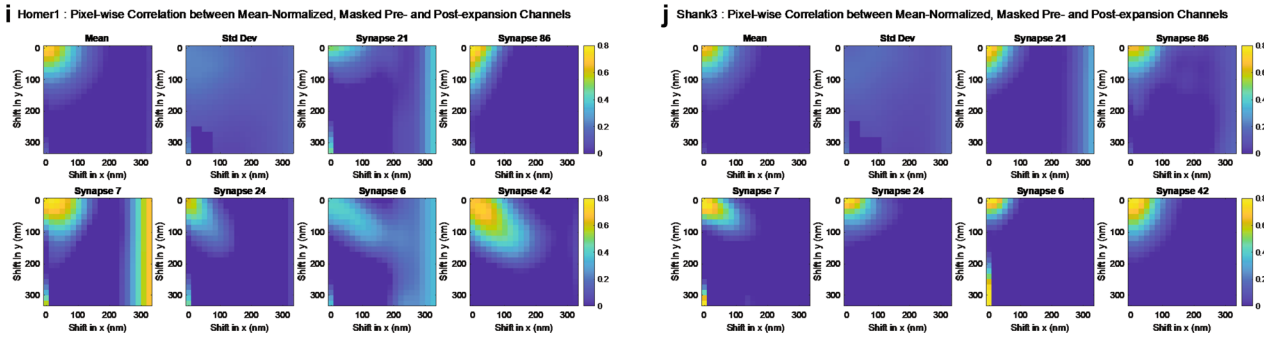

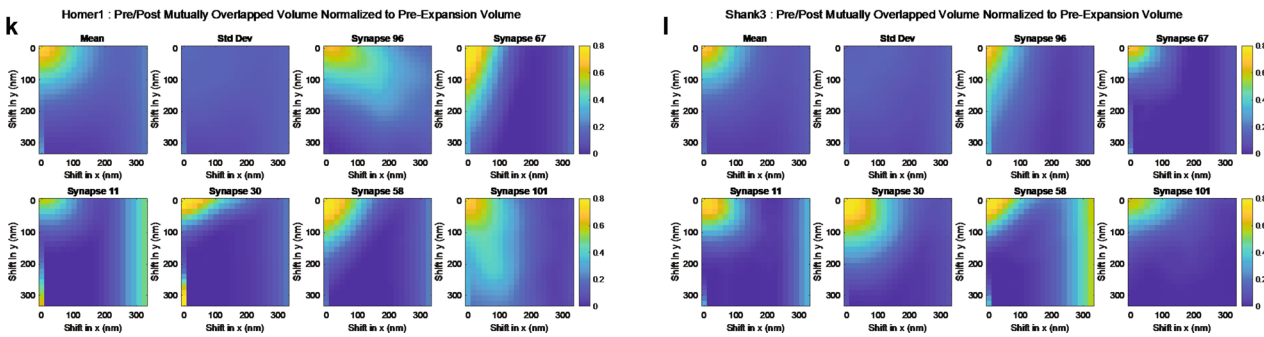

Extended Data Fig. 3 | See next page for caption.

Extended Data Fig. 3 | Analysis of the distortion caused by post-expansion staining, as compared to classical pre-expansion staining. (a-b) Representative background-subtracted and binary images of Homer1 **(a)** and Shank3 **(b)** in pre- and post-expansion staining channels (top row (yellow): pre-expansion channel, second row (black/white): binary pre-expansion channel, third row (magenta): post-expansion channel, bottom row (black/white): binary post-expansion channel). **(c)** Number of synaptic puncta for pre- and post-expansion staining channels, after filtration, for the images in (a-b). **(d)** Population distribution (violin plot of density, with a dashed line at the median and dotted lines at the quartiles) of the number of synaptic puncta in the pre-expansion staining channel for Homer1 and Shank3 (see Supplementary Table 5 for statistics for this figure). **(e)** Population distribution of the number of synaptic puncta in the post-expansion staining channel for Homer1 and Shank3. **(f)** Difference in the number of synaptic puncta between post- and pre-expansion staining channels normalized to the number of synaptic puncta in the pre-expansion staining channel. (g-h) Pixel-wise autocorrelation between pre-expansion (pre-pre, yellow), post-expansion (post-post, magenta), and pixel-wise correlation between pre- and post-expansion (pre-post, black) as a function of shift distance in x- (left column), y- (middle column), and z- (right column) directions for Homer1 **(g)** and Shank3 **(h)**. The mean across all synapses is shown in the top row, and representative synapses are shown in the second through fourth rows. These values were used to calculate the linearized error measure shown in Extended Data Fig. 2f, g. (i-j) Pixel-wise correlation between mean-normalized, masked pre- and post-expansion channels as a function of shift distance in x- and y-directions ($z=1$) for Homer1 **(i)** and Shank3 **(j)**. The mean across all synapses is shown in the top left, standard deviation across all synapses shown in second from the top left, and representative synapses are shown in the remaining plots. (k-l) Mutually overlapped volume between pre- and post-expansion stained synaptic puncta, normalized to total puncta volume in the pre-expansion staining channel, as a function of shift distance in x- and y-directions ($z=1$) for Homer1 **(k)** and Shank3 **(l)**. The mean across all synapses is shown in the top left, standard deviation across all synapses shown in second from the top left, and representative synapses are shown in the remaining plots. Analysis was conducted on 480 (before exclusion based on size) synapses for Shank3 and Homer1 from 3 mice (see Supplementary Table 5 for exact numbers).

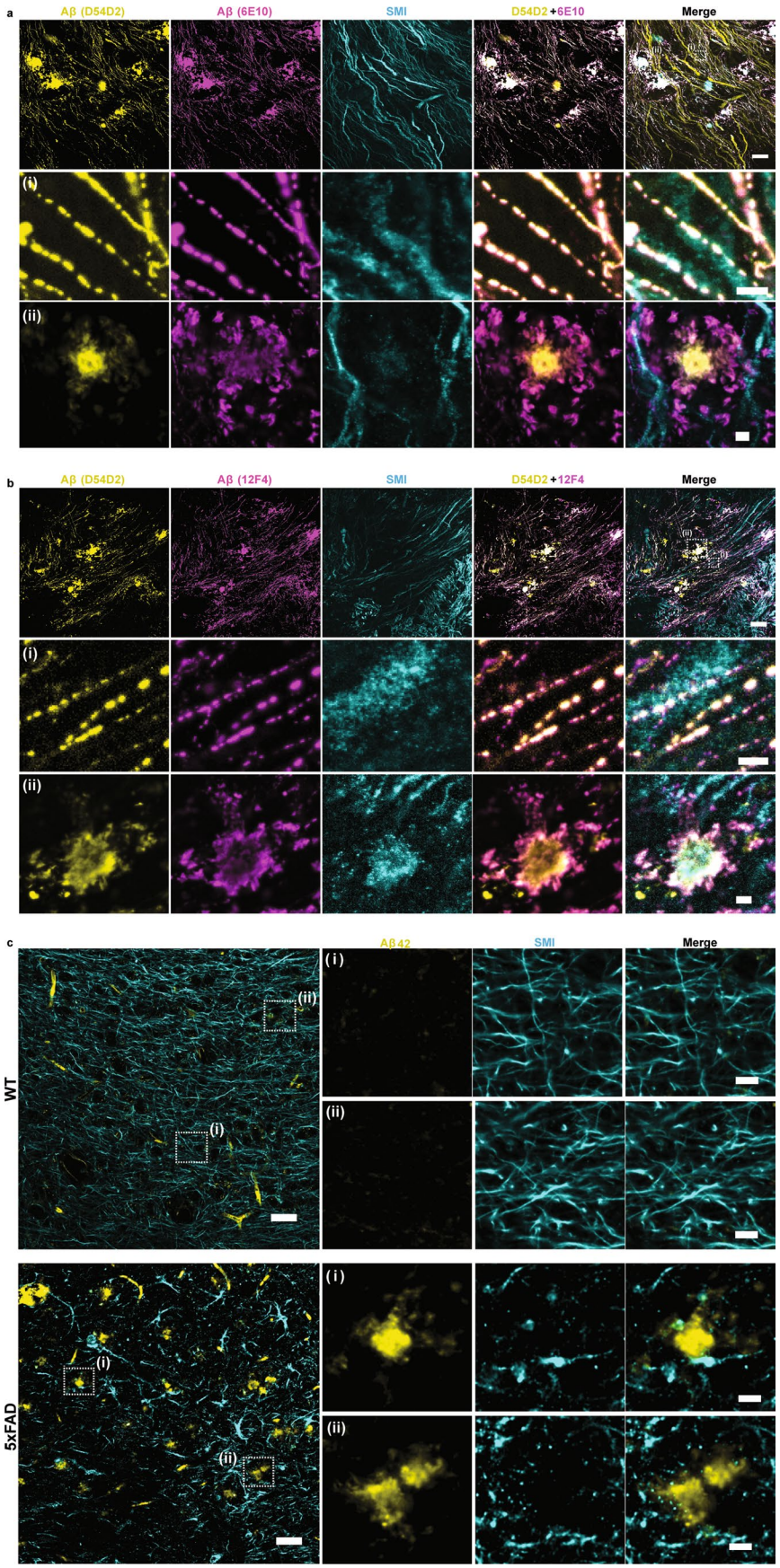

Extended Data Fig. 4 | See next page for caption.

Extended Data Fig. 4 | ExR and unexpanded tissue confocal images showing immunolabeling of Aβ42. ExR confocal images (single z-slices) showing immunolabeling of Aβ42 with two different monoclonal antibodies **(a)** D54D2 + 6E10 and **(b)** D54D2 + 12F4 with SMI co-staining in the fornix of 5xFAD mouse (n = 3 fields of view of 2 slices from 2 mice). Scale bar, 10 μm (top row), 1 μm (i, ii panels). **(c)** Unexpanded tissue confocal image, a single z-slice, showing pre-expansion Aβ42 (yellow) and SMI (cyan) staining in the fornix of WT (upper panel) and 5xFAD mice (lower panel) (n = 3 fields of view of 1 slice from 1 mouse per WT and 5xFAD, respectively). Scale bar, 30 μm (left panel) and 6 μm (panels i, ii)).

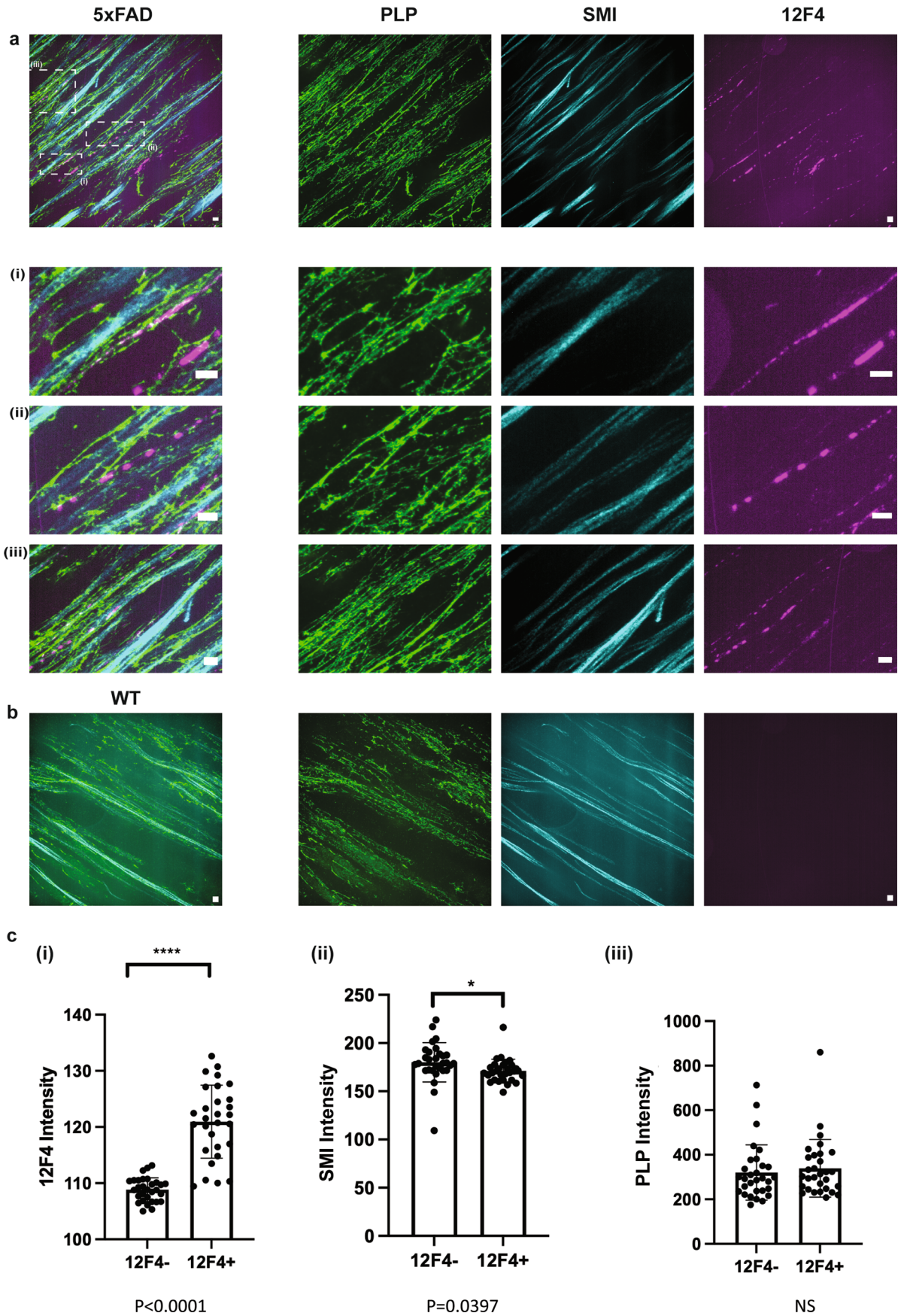

Extended Data Fig. 5 | See next page for caption.

Extended Data Fig. 5 | ExR confocal images showing immunolabeling of PLP, SMI, and 12F4 in 5xFAD and WT fornix. ExR reveals relative localization of Aβ42 peptide and myelin in the fornix of Alzheimer's model 5xFAD and WT mice (n = 2 fields of view of 1 slice from 2 mice per WT and 5xFAD, respectively). **(a)** ExR confocal image (max intensity projections, 900–1000 nm thickness) showing post-expansion Aβ42 (magenta), SMI (cyan) and PLP (green) staining in the fornix of 5xFAD mice. Leftmost panel, merged low-magnification image; right images show individual channels. Insets (i-iii) show close-up views of the boxed regions highlighted in the upper left image. **(b)** ExR confocal image (max intensity projections, 1.72 μm thickness) showing post-expansion Aβ42 (magenta), SMI (cyan) and PLP (green) staining in the fornix of wild-type mice. Leftmost panel, merged image. All images were subtracted background using Fiji's Rolling Ball algorithm with radius 50 pixels, and adjusted with auto-contrast. Scale bar = 500 nm. **(c)** Comparison of 12F4, SMI, and PLP intensity levels along axons in 5xFAD fornix with and without 12F4. To analyze axonal amyloid beta deposition with myelination and SMI intensity, we measure the (i) 12F4, (ii) SMI and (iii) PLP intensity levels along 10 axons with (12F4+) and without 12F4 (12F4-) from the same field of view (n = 3 fields of view of 2 slices from 2 5xFAD). All images were subtracted background with 50 pixels, and adjusted with auto-contrast for analysis by ImageJ. On each axon, three lines were drawn cross-sectionally across each axon in Image J and averaged intensity levels of PLP, 12F4 and SMI from different channels were measured respectively along these lines. For 12F4 + axons, each line was drawn across the centroid of amyloid beta deposition. For 12F4- axons, lines were positioned randomly along the axon. We then compared PLP, 12F4 and SMI312 intensity levels between 12F4 + and 12F4- axons. Plotted is the mean, with error bars representing standard error of the mean (SEM). Two-sided paired t-test, (i) ****$p < 0.0001$, $t = 6.112$, $df = 18$, (ii) $p = 0.0595$, $t = 2.012$, $df = 18$, (iii) $p = 0.6580$, $t = 0.4502$, $df = 18$.

nature research

Corresponding author(s): E. Boyden, L-H. Tsai and T. Blanpied

Last updated by author(s): Jun 1, 2022

Reporting Summary

Nature Research wishes to improve the reproducibility of the work that we publish. This form provides structure for consistency and transparency in reporting. For further information on Nature Research policies, see our Editorial Policies and the Editorial Policy Checklist.

Statistics

For all statistical analyses, confirm that the following items are present in the figure legend, table legend, main text, or Methods section.

n/a	Confirmed	
☐	☒	The exact sample size (*n*) for each experimental group/condition, given as a discrete number and unit of measurement
☐	☒	A statement on whether measurements were taken from distinct samples or whether the same sample was measured repeatedly
☐	☒	The statistical test(s) used AND whether they are one- or two-sided *Only common tests should be described solely by name; describe more complex techniques in the Methods section.*
☐	☒	A description of all covariates tested
☐	☒	A description of any assumptions or corrections, such as tests of normality and adjustment for multiple comparisons
☐	☒	A full description of the statistical parameters including central tendency (e.g. means) or other basic estimates (e.g. regression coefficient) AND variation (e.g. standard deviation) or associated estimates of uncertainty (e.g. confidence intervals)
☐	☒	For null hypothesis testing, the test statistic (e.g. *F*, *t*, *r*) with confidence intervals, effect sizes, degrees of freedom and *P* value noted *Give P values as exact values whenever suitable.*
☒	☐	For Bayesian analysis, information on the choice of priors and Markov chain Monte Carlo settings
☒	☐	For hierarchical and complex designs, identification of the appropriate level for tests and full reporting of outcomes
☒	☐	Estimates of effect sizes (e.g. Cohen's *d*, Pearson's *r*), indicating how they were calculated

Our web collection on statistics for biologists contains articles on many of the points above.

Software and code

Policy information about availability of computer code

Data collection	Raw image data were collected by a Nikon Eclipse Ti inverted microscope with NIS-Elements software.
Data analysis	Fiji/ImageJ and custom MATLAB (versions R2014, R2019a-b, and R2020a-b) scripts were used to process images. Python 3 was used for some statistical analyses. The code is available on Zenodo at DOI:10.5281/zenodo.6383293 and on Github at https://github.com/schroeme/ExR.

For manuscripts utilizing custom algorithms or software that are central to the research but not yet described in published literature, software must be made available to editors and reviewers. We strongly encourage code deposition in a community repository (e.g. GitHub). See the Nature Research guidelines for submitting code & software for further information.

Data

Policy information about availability of data

All manuscripts must include a data availability statement. This statement should provide the following information, where applicable:

- Accession codes, unique identifiers, or web links for publicly available datasets
- A list of figures that have associated raw data
- A description of any restrictions on data availability

The main data supporting the results in this study are available within the paper and its Supplementary Information. The raw and analysed datasets generated during the study are too large to be publicly shared, yet they are available for research purposes from the corresponding authors on reasonable request.

Field-specific reporting

Please select the one below that is the best fit for your research. If you are not sure, read the appropriate sections before making your selection.

☒ Life sciences ☐ Behavioural & social sciences ☐ Ecological, evolutionary & environmental sciences

For a reference copy of the document with all sections, see nature.com/documents/nr-reporting-summary-flat.pdf

Life sciences study design

All studies must disclose on these points even when the disclosure is negative.

Sample size	The studies were done with 1 or more mouse specimens with 2 or more fields of view each.
Data exclusions	Some synapses were excluded from analysis. Criteria for exclusion are detailed in Methods. We identified measured signal from one field of view from one animal as an outlier using the ROUT method with Q=1% in GraphPad Prism, and excluded it from further analysis and visualization.
Replication	All attempts at replication were successful.
Randomization	Randomization was not relevant to the study because the synapse staining of the somatosensory cortex was obtained from one strain (C57BL/6), and the amyloid-beta staining was obtained from 5xFAD, with WT as a control.
Blinding	Blinding was not relevant to most of the study because the synapse staining of the somatosensory cortex (L1, L2/3, L4) was imaged as is, and simply analysed after taking images, and because there are obvious differences in WT and 5xFAD tissues regarding the presence of amyloid plaques. The investigators were blinded to the groups for analysis of the layer-specific synaptic nanocolumn dataset (Fig. 3).

Reporting for specific materials, systems and methods

We require information from authors about some types of materials, experimental systems and methods used in many studies. Here, indicate whether each material, system or method listed is relevant to your study. If you are not sure if a list item applies to your research, read the appropriate section before selecting a response.

Materials & experimental systems

n/a	Involved in the study
☐	☒ Antibodies
☒	☐ Eukaryotic cell lines
☒	☐ Palaeontology and archaeology
☐	☒ Animals and other organisms
☒	☐ Human research participants
☒	☐ Clinical data
☒	☐ Dual use research of concern

Methods

n/a	Involved in the study
☒	☐ ChIP-seq
☒	☐ Flow cytometry
☒	☐ MRI-based neuroimaging

Antibodies

Antibodies used	Antibody information, including supplier names and catalogue numbers, is provided in the Supplementary Information.
Validation	Information on the validation of each primary antibody was provided on the manufacturer's website. All antibodies used in the study are commercially available.

Animals and other organisms

Policy information about studies involving animals; ARRIVE guidelines recommended for reporting animal research

Laboratory animals	Both male and female wild-type mice (C57BL/6 or Thy1-YFP, 6-8 weeks) and 5xFAD mice (12–13 months) were used.
Wild animals	The study did not involve wild animals.
Field-collected samples	The study did not involve samples collected from the field.

Ethics oversight	All procedures involving animals were in accordance with the U.S. National Institutes of Health Guide for the Care and Use of Laboratory Animals, and approved by the Massachusetts Institute of Technology Committee on Animal Care.

Note that full information on the approval of the study protocol must also be provided in the manuscript.